Technische Universität München
Fakultät für Luftfahrt, Raumfahrt und Geodäsie
Lehrstuhl für Methodik der Fernerkundung

Compensation of atmospheric disturbances in differential interferometry by adoption of high resolution weather models

Franz–Georg Ulmer

Vollständiger Abdruck von der Fakultät für Luftfahrt, Raumfahrt und Geodäsie der Technischen Universität München zur Erlangung des akademischen Grades eines **Doktor-Ingenieurs (Dr.-Ing.)** genehmigten kumulativen Dissertation.

Vorsitzende:

Prof. Dr.-Ing. habil. Xiaoxiang Zhu

Prüfende der Dissertation:

1. Prof. Dr.-Ing. habil. Richard Bamler
2. Hon. Prof. Dr. rer. nat. Michael Eineder
3. apl. Prof. Dr. Thomas R. Walter

Die kumulative Dissertation wurde am 14.05.2020 bei der Technischen Universität München eingereicht und durch die Ingenieurfakultät für Luftfahrt, Raumfahrt und Geodäsie am 15.12.2020 angenommen.

Dedicated to my loving family.

Acknowledgement: I would like to thank all my colleagues for their support and all co-authors who made this cumulative dissertation possible. Explicitly, I would like to thank Nico Adam for providing essential source code basis transforming weather model data into an atmospheric phase screen, for teaching scientific writing as well as for the substantial support writing and correcting the papers and guiding through the reviews.

Abstract

Differential interferometric SAR is a popular remote sensing technique to monitor deformations of the earth surface. However, the atmosphere disturbs interferograms and therefore affects the deformation estimate. The disturbance is reduced, by using a time series analysis of interferograms. The quality of the deformation estimate depends on the magnitude of the disturbance and the time series length. Correspondingly, the quality increases, or the necessary time series length is reduced to achieve a certain quality level, by reducing the disturbance magnitude. In order to achieve this, Numerical weather predictions (NWP) can be utilised to hindcast the atmospheric states during SAR acquisitions which in turn are mapped into disturbance estimates. Such a disturbance map is denoted in research publications and in this work as atmospheric phase screen (APS). APS estimates are subtracted from interferograms to reduce the perturbation and improve the starting conditions for time series analysis. However, the quality of the hindcast and respectively the quality of the APS estimate depends on the NWP setup and the quality of the initialization data.

An important NWP characteristic is the forecast duration and the related APS estimate quality. This cumulative dissertation reports a best forecast duration of between 6 - 12 hours. Further, the digital initialization technique that reduces initial imbalances, improves the forecasts exclusively within the first 4 hours. Correspondingly, the additional computational effort is not justified for the desired application.

The structure functions of estimated APSs and interferograms show a discrepancy in the research publications. This cumulative dissertation explains the discrepancy that results from the much coarser resolution of the forecasts compared to interferograms and the noise that is present in interferograms. An alternative statistical analysis is provided that overcomes the structure function limitations. The derived characteristics indicate an agreement between predicted APSs and observed interferograms and allow the effective resolution of numerical weather predictions for APS mitigation to be determined. Further, the derived characteristics from predicted APSs can be used to support the time series analysis.

Ensemble NWPs reflect the uncertainties of hindcasts. Correspondingly, a

weighted ensemble mean represent the expected atmospheric state, if the weights are related to the uncertainties of the ensemble members. An algorithm is proposed, in this cumulative dissertation, that fits predicted atmospheric phase screens to the interferogram in a root mean square sense. This technique improves the atmospheric phase screen mitigation by about 40 % compared to the straight forward technique and improves the pressure prediction by using the derived coefficients for the weighted ensemble mean.
The peer reviewed full-paper publications

1. [Ulmer and Balss, 2016] *Spin-up time research on the weather research and forecasting model for atmospheric delay mitigations of electromagnetic waves* published in *Journal of Applied Remote Sensing*

2. [Ulmer, 2016] *On the accuracy gain of electromagnetic wave delay predictions derived by the digital filter initialization technique* published in *Journal of Applied Remote Sensing*

3. [Ulmer and Adam, 2017] *Characterisation and improvement of the structure function estimation for application in psi* published in *ISPRS Journal of Photogrammetry and Remote Sensing*

4. [Ulmer and Adam, 2015] *A synergy method to improve ensemble weather predictions and differential sar interferograms* published in *ISPRS Journal of Photogrammetry and Remote Sensing*

sum up this cumulative dissertation.

Keywords: atmopheric phase delay, APS compensation, high resolution weather model, NWP, water vapour

Contents

List of Figures

List of Tables

Chapter 1

Introduction

Differential interferometry is a very sensitive remote sensing technique that is commonly used to observe deformations of the Earths surface. A short electromagnetic wave is transmitted by an SAR satellite which is scattered back to the SAR sensor. The phase information of the received electromagnetic wave is related to the distance of a scatterer to the SAR sensor. Unfortunately, the wave propagation velocity is affected by the refractive index of air which can be characterised by pressure, temperature and humidity. Therefore, the atmosphere affects the phase information and disturbs the distance measurement. To be precise, differential interferometry subtracts two phase measurements. The measurements may come from two SAR sensors which acquire the surface simultaneously or from one SAR sensor that acquires the surface repeatedly. In the first scenario, the atmospheric disturbance is corrected automatically, because both measurements are affected by the disturbance in the same way. Unfortunately, the measurements are affected differently in the second scenario because the atmospheric conditions differ. Hence, the atmospheric disturbance should be compensated. This can be done by time series analysis and preprocessing steps that utilize numerical weather predictions (NWP) to estimate the disturbance and correct the interferograms. However, this preprocessing is not straight forward due to the chaotic nature of the atmosphere, the various available NWP models and initialization data sets, and various parametrizations of the NWP. This work lists different NWP models, describes their aim and goals and provides an overview of initialization data sets and investigates how to deal with this large degree of freedom and provides a cost effective

setting for operational usage.

The work is structured as follows. Firstly, the theory of the refractive index and the related time delay estimation is described. Secondly, an introduction to numerical weather prediction models and its initialisation data is given. Thirdly, an overview is provided of the literature dealing with APS compensation utilising NWPs. Fourthly, an overview of my published works is given. Fifthly, the synoptic discussion links these works together and describes how a cost effective operational service for atmospheric phase screen correction can be achieved.

Chapter 2

Delay theory of the atmosphere

The atmosphere causes time- and space-variant delay variations of electromagnetic waves and therefore effects differential interferograms. Physically, this process is described by the refractive index which is defined by the fraction of speed of light and wave propagation velocity within a matter. In our case, this matter is air and is in this area of expertise separated into two parts. Firstly, the non-polar gas component and secondly the polar gas component. The refractive index of the non-polar gas component is approximated by a linear function while the polar gas component is approximated by a quadratic polynomial of temperature and pressure. Both approximations together form a final approximation named as refractivity. In satellite interferometry the refractivity is integrated along the line of sight of the SAR satellite to derive an estimate of the atmospheric delay for electromagnetic waves.
Several approximations are reported in research publications and are easily confused. Therefore, the different refractivity approximations are now derived to distinguish and to discuss them.

2.1 Dielectric spectroscopy

Starting with the physical cause, the different approximations of the refractivity are now derived. A dielectric material is an electrical isolator which can be polarized. It could be a gas, a fluid or a solid matter. If an electromagnetic field goes through this material, no electrons will flow as is known from conductors.

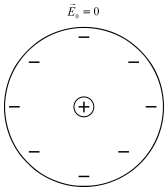

Figure 2.1: Electromagnetic polarization without an electromagnetic field. Graphic from Wikipedia [uploaded by Kakashi-Madara, 2009a].

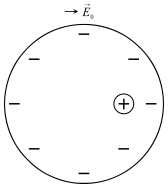

Figure 2.2: Electromagnetic polarization with an electromagnetic field. Graphic from Wikipedia [uploaded by Kakashi-Madara, 2009b].

A reduction of the electromagnetic field occurs and is measured by permittivity. The dielectric spectroscopy measures the dielectric characteristics dependent on the frequency expressed by permittivity. The result of an electromagnetic field is a polarization of the penetrated material which could be divided into four classes.

1. **Electromagnetic polarization** occurs if the electron hull is shifted (see Figures 2.1 vs. 2.2)
2. **Atomic polarization** occurs if the electron hull is deformed (see Figure 2.3)
3. **Dipole relaxation** occurs if the electromagnetic field orders the atoms (see Figures 2.5 vs. 2.6)
4. **Ionic relaxation** occurs if the electromagnetic field changes the ionic distribution (see Figures 2.7 vs. 2.8)

The whole interaction of these effects influences the permittivity which is described by the following theorem. For this, the dielectric constant (ϵ) is defined by the fraction of the permittivity of the corresponding material and the vacuum. The following theory is from Bean and Dutton [1966].

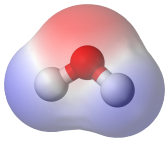

Figure 2.3: Bent electron hull of a water molecule (polar shape). Graphic from Wikipedia [uploaded by Mills, 2006].

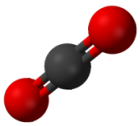

Figure 2.4: Carbon dioxide has two bond dipole moments which are canceled out because of the linear geometry of the molecule. Graphic from Wikipedia [uploaded by Benji9072, 2010].

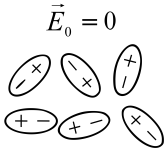

Figure 2.5: Electromagnetic polarization without an electromagnetic field. Graphic from Wikipedia [uploaded by Kakashi-Madara, 2009c].

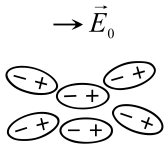

Figure 2.6: Electromagnetic polarization with an electromagnetic field. Graphic from Wikipedia [uploaded by Kakashi-Madara, 2009d].

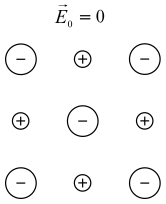

Figure 2.7: Electromagnetic polarization without an electromagnetic field. Graphic from Wikipedia [uploaded by Kakashi-Madara, 2009e].

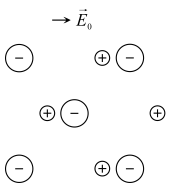

Figure 2.8: Electromagnetic polarization with an electromagnetic field. Graphic from Wikipedia [uploaded by Kakashi-Madara, 2009f].

Scientific law 2.1.1 (See Bean and Dutton [1966]:). *The* ***polarization****, P, of a polar matter under the influence of a high-frequency radio field is given by:*

$$P(\omega) = \frac{\epsilon - 1}{\epsilon + 2}\frac{M}{\rho} = \frac{4\pi N}{3}\left(\alpha_0 + \frac{\mu^2}{3kT}\frac{1}{1 + i\omega\tau}\right)$$

where
- ϵ *is the dielectric constant,*
- M *is the molecular weight,*
- ρ *is the density of the matter,*
- N *is Avogadro's number,*
- α_0 *is the average polarizability of the molecules in the matter, assuming no interaction between molecules,*
- μ *is the permanent dipole moment,*
- k *is Bolzmann's constant,*
- T *is the absolute temperature,*
- τ *is the relaxation time required for external field-induced orientations of the molecules to return to random distribution after the field is removed,*
- ω $= 2\pi f$ *where f is the frequency of the external field.*

Which is written for frequencies less than 100 GHz ($\omega\tau << 1$) to

$$\frac{\epsilon - 1}{\epsilon + 2}\frac{M}{\rho} = \frac{4\pi N}{3}\left(\alpha_0 + \frac{\mu^2}{3kT}\right). \tag{2.1}$$

Polar molecules have a deformed electron hull whereas non-polar molecules have no dipole moment (compare Figures 2.4 and 2.3). Hence, non-polar gases are characterized by $\mu = 0$ and polar gases by $\mu > 0$. Therefore, the following equations describe the more complex case of polar gases and are finally simplified for non-polar gases.
For simplicity, Equation 2.1 is shortened to

$$\frac{\epsilon - 1}{\epsilon + 2}\frac{M}{\rho} = \frac{4\pi N}{3}\left(\alpha_0 + \frac{\varkappa}{T}\right). \tag{2.2}$$

where $\varkappa = \frac{\mu^2}{3k}$. Since air has a dielectric constant of about one ($\epsilon \approx 1$), the following approximation is valid

$$\epsilon - 1 \approx \frac{4\pi N\rho}{M}\left(\alpha_0 + \frac{\varkappa}{T}\right). \tag{2.3}$$

For the next step we have to use the ideal gas law.

Scientific law 2.1.2 (See Moran and Shapiro [2009]:). *The* ***ideal gas law*** *is described by:*

$$PV = nRT$$

where P *is the pressure,*
V *is the volume,*
n *is the amount of substance,*
R *is the universal gas constant,*
T *is the absolute temperature.*

Let m be the mass, then equation 2.3 becomes with theorem 2.1.2 to

$$\begin{aligned}
\epsilon - 1 &\approx \frac{4\pi N\rho}{M}\left(\alpha_0 + \frac{\varkappa}{T}\right) && (2.4)\\
&= 4\pi\frac{N\frac{m}{V}}{M}\left(\alpha_0 + \frac{\varkappa}{T}\right) && (2.5)\\
&= 4\pi\frac{N\frac{m}{M}}{V}\left(\alpha_0 + \frac{\varkappa}{T}\right) && (2.6)\\
&= 4\pi\frac{Nn}{V}\left(\alpha_0 + \frac{\varkappa}{T}\right) && (2.7)\\
&= K\frac{P}{T}\left(\alpha_0 + \frac{\varkappa}{T}\right) && (2.8)\\
&= K_1\frac{P}{T} + K_2\frac{P}{T^2} && (2.9)
\end{aligned}$$

where $K = 4\pi\frac{N}{R}, K_1 = K\alpha_0$ and $K_2 = K\varkappa$ are constants. For non-polar gases ($\varkappa = 0$) this approximation is simplified to

$$\epsilon - 1 \approx K_1\frac{P}{T}. \tag{2.10}$$

Next, for a mixture of polar and non-polar gases Dalton's law of partial pressures is assumed.

Scientific law 2.1.3 (See Silberberg [2009]:)**.** ***Dalton's law of partial pressures*** *states that the sum of the partial pressures equals the total pressure:*

$$P_{total} = \textstyle\sum_i P_i$$

where P_i is the partial pressure of each component. It is assumed that the gases do not react with each other.

In doing so, this results in the fact that the dielectric constant can be the sum of polar and non-polar gases and hence obtain

$$\epsilon - 1 \approx \underbrace{\sum_i K_{1_i}\frac{P_i}{T}}_{\text{non-polar mixture}} + \underbrace{\sum_j \left(K_{1_j}\frac{P_j}{T} + K_{2_j}\frac{P_j}{T^2}\right)}_{\text{polar mixture}}. \tag{2.11}$$

Commonly, pressure of air is divided into the partial pressures of non-polar gases dry air (P_d), CO_2 (P_c), and the polar gas water vapour (e). This leads to

$$\epsilon - 1 \approx K_{1_d}\frac{P_d}{T} + K_{1_c}\frac{P_c}{T} + K_{1_e}\frac{e}{T} + K_{2_e}\frac{e}{T^2}. \tag{2.12}$$

The CO_2 concentration in the air varies depending on the position on Earth. However, for simplicity, a fixed CO_2 concentration is often assumed, thus the two non-polar gas terms are combined. In doing so, the equation is simplified to

$$\epsilon - 1 \approx K_{1_{dc}} \frac{P_{dc}}{T} + K_{1_e} \frac{e}{T} + K_{2_e} \frac{e}{T^2} \tag{2.13}$$

where P_{dc} is the partial pressure of dry air with a fixed CO_2 concentration ratio.

2.2 Refraction

An approximation of the dielectric constant was derived in 2.1 dependent on partial pressures and temperature. The dielectric constant is related to the refractive index that allows a first representation of the refractive formula depending on partial pressures and temperature to be derived.

2.2.1 First representation of the refractive formula

The refractive index describes the relative velocity of an electromagnetic wave within a material relative to the vacuum.

Definition 2.2.1 (Hecht [2002])**.** *The refractive index of an material m is defined by:*

$$n_m = \frac{c}{v_m}$$

where v_m is the velocity of the wave propagation through the material and the speed of light.

The relationship between the refractive index and the dielectric constant is [see Bean and Dutton, 1966]

$$n = \sqrt{\mu\epsilon} \tag{2.14}$$

$$\Leftrightarrow \quad n^2 = \mu\epsilon \tag{2.15}$$

$$\Leftrightarrow \quad \epsilon = \frac{n^2}{\mu} \tag{2.16}$$

where μ is the permanent dipole moment. It is not surprising, that the refractive index of air is approximately 1 since the wave propagation in air is nearly c. Because of this, a Taylor series approximation of second degree of ϵ for supporting point $n = 1$ is derived from Equation 2.16. It is

$$\epsilon \approx \frac{1}{\mu} + \frac{2}{\mu}(n-1) \tag{2.17}$$

$$= \frac{1}{\mu}\Big(1 + 2(n-1)\Big) \tag{2.18}$$

$$= \frac{1}{\mu}(2n-1) \tag{2.19}$$

$$\Leftrightarrow \quad \epsilon\mu \approx 2n - 1 \tag{2.20}$$

$$\Leftrightarrow \quad \frac{\epsilon\mu}{2} \approx n - \frac{1}{2} \tag{2.21}$$

$$\Leftrightarrow \quad \frac{\epsilon\mu - 1}{2} \approx n - 1. \tag{2.22}$$

Using equation 2.12 and assuming $\mu = 1$ which is very close to the actual value $\mu \approx 1.00000037$ [see Cullity and Graham, 2008], the first representation of the refractivity follows [1]

$$N = (n-1) \times 10^6 = K_1\frac{P_d}{T} + K_2\frac{e}{T} + K_3\frac{e}{T^2} + K_4\frac{P_c}{T} \tag{2.23}$$

where K_1, K_2, K_3 and K_4 are new constants. N is named as refractivity or scaled refractivity because of the 10^6 factor.

Since the derived Equation 2.23 is based on an acknowledged physical model, one can expect that the presented formula fits well to the reality. On the one hand, measured delay variations, temperatures and partial pressures allow to be adjusted. On the other hand, known coefficients, partial pressures and temperature allow the delay caused by the atmosphere to be estimated. A detailed description of the estimation of this delay will be presented later.

2.2.2 Extended formula with compressibility factors

An extended version of equation 2.23 was introduced by Owens [1967]. Compressibility factors were added, allowing the ideal gas law assumption to be

[1] Here, N is not the avogadro number already used above. This notation was chosen to maintain a notation with other literature.

overcome. Accordingly, a more accurate model of refractivity is achieved whereby a more accurate estimate of the atmospheric delay can be achieved.

Definition 2.2.2 (Davis et al. [1985]:). *The compressibility factor of gas i is defined by*

$$Z_i = \frac{P_i}{\rho_i R_i T}$$

where P_i is the partial pressure, ρ_i mass density, R_i specific gas constant and T is the temperature. Furthermore is $R_i = \frac{R}{M_i}$ where R is the universal gas constant and M_i the molar mass.

This equation is rewritten to

$$Z_i = \frac{M_i P_i}{\rho_i R T} \tag{2.24}$$

which leads to

$$\rho_i = \frac{M_i P_i}{RT} Z_i^{-1}. \tag{2.25}$$

By substituting ρ into equation 2.3 by equation 2.25 and add the index i to distinguish different gases, the approximation 2.9 becomes to

$$\epsilon_i - 1 \approx \frac{4\pi N}{M_i} \frac{M_i P_i}{RT} Z_i^{-1} \left(\alpha_{0i} + \frac{c_i}{T}\right) = K_{i1} \frac{P_i}{T} Z_i^{-1} + K_{i2} \frac{P_i}{T^2} Z_i^{-1} \tag{2.26}$$

By doing this and reevaluating Equations 2.9 to 2.23 leads to the refractivity Equation with compressibility factors

$$N = (n-1) \times 10^6 = K_1 \frac{P_d}{T} Z_d^{-1} + K_2 \frac{P_c}{T} Z_c^{-1} + K_3 \frac{e}{T} Z_e^{-1} + K_4 \frac{e}{T^2} Z_e^{-1} \tag{2.27}$$

where Z_d, Z_c, Z_e are the compressibility factors of dry air, CO_2 and water vapour respectively.

2.2.3 The dry and wet term separation

As already mentioned, to derive Equation 2.13, the dry term and the CO_2 term are often combined. By doing this the refractivity is separated into a non-polar and a polar gas component. In literature, these two terms commonly are marked as the **dry** and the **wet** term respectively. The refractivity in its general form is now

$$N = (n-1) \times 10^6 = \underbrace{K_1 \frac{P_{dc}}{T} Z_{dc}^{-1}}_{\text{dry}} + \underbrace{K_2 \frac{e}{T} Z_e^{-1} + K_3 \frac{e}{T^2} Z_e^{-1}}_{\text{wet}} \tag{2.28}$$

where $P_{dc} = P_c + P_d$ and Z_{dc} is the corresponding compressibility factor. The constant K_1 differs to those in equation 2.27 and 2.23.

2.2.4 The hydrostatic and non-hydrostatic term separation

Another common representation of the refractivity is the **hydrostatic** and **non-hydrostatic** term separation. The hydrostatic term depends on the total pressure (P) (for an ideal gas) or total density (for a non-ideal gas) (ρ) instead of partial pressure (P_{dc}) or partial density (ρ_{dc}). Correspondingly, the non-hydrostatic component follows from the hydrostatic term definition which is described in detail now.

The hydrostatic and non-hydrostatic term separation for an ideal gas

Equation 2.28 is rewritten and an ideal gas is assumed ($Z_{dc}^{-1} = 1$, $Z_e^{-1} = 1$) that

$$\begin{aligned} N &= K_1 \frac{P_{dc}}{T} + K_2 \frac{e}{T} + K_3 \frac{e}{T^2} && (2.29) \\ &= K_1 \frac{P-e}{T} + K_2 \frac{e}{T} + K_3 \frac{e}{T^2} && (2.30) \\ &= K_1 \frac{P}{T} - K_1 \frac{e}{T} + K_2 \frac{e}{T} + K_3 \frac{e}{T^2} && (2.31) \\ &= \underbrace{K_1 \frac{P}{T}}_{\text{hydrostatic}} + \underbrace{K_2' \frac{e}{T} + K_3 \frac{e}{T^2}}_{\text{non-hydrostatic}}. && (2.32) \end{aligned}$$

Note, $K_2' = K_2 - K_1$ represents a new variable and should not be confused with K_2.

The hydrostatic and non-hydrostatic term separation for a non-ideal gas

For a non ideal gas, Davis et al. [1985] introduced this formula by rewriting the first two terms of 2.28 using definition 2.2.2

$$K_1 \frac{P_{dc}}{T} Z_{dc}^{-1} + K_2 \frac{e}{T} Z_e^{-1} = K_1 R_{dc} \rho_{dc} + K_2 R_e \rho_e \tag{2.33}$$

$$= K_1 R_{dc} \rho + K_2' \frac{e}{T} Z_e^{-1} \tag{2.34}$$

where $\rho = \rho_{dc} + \rho_e$ is the total mass density. Again, K_2' is differently defined and is this time

$$K_2' = K_2 - K_1 \frac{R_{dc}}{R_e}. \tag{2.35}$$

Finally equation 2.28 becomes

$$N = (n-1) \times 10^6 = \underbrace{K_1 R_{dc} \rho}_{\text{hydrostatic}} + \underbrace{K_2' \frac{e}{T} Z_e^{-1} + K_3 \frac{e}{T^2} Z_e^{-1}}_{\text{non-hydrostatic}}. \tag{2.36}$$

Because of the different representations of the refractivity (dry / wet, hydrostatic / non-hydrostatic for (non-) ideal gasses) different constants with same nomenclature are present in literature [for example Rüeger, 2002, Davis et al., 1985, Smith and Weintraub, 1953, Thayer, 1974] and are therefore easy to mix up.

2.2.5 Model decision and parametrisation

The total delay of the electromagnetic wave in air is independent of the separation chosen for representation of refractivity. Therefore, the separation / representation which is used to derive the total delay is a personal design decision. However, there are two advantages of the hydrostatic / non-hydrostatic separation compared to the dry / wet separation. This is because the total pressure ($P = P_{dc} + e$) is nearly constant within a short range at the same altitude, but the water vapour partial pressures e vary therein because of the chaotic nature of convection. Correspondingly, the dry / wet delay terms of two close range-azimuth positions vary while the hydrostatic delay term is much

more stable compared to the dry term. Another advantage of the hydrostatic delay term is that it could be estimated robustly from the surface pressure [see Davis et al., 1985]. Because of these two advantages of the hydrostatic delay term, the hydrostatic / non-hydrostatic delay separation is used within this work. The corresponding coefficients are

$$K_1 = 77.6890\text{K / mbar} \tag{2.37}$$

$$K_2' = -6.3938\text{K / mbar} \tag{2.38}$$

$$K_3 = 3.75463 \times 10^5 \text{K}^2/\text{mbar} \tag{2.39}$$

and where taken from [Rüeger, 2002].

2.3 The ray path through the atmosphere

If an electromagnetic wave propagates through the atmosphere, it is diverted and delayed because of the refractive index. Both effects are now described.

2.3.1 The ray bending effect

If an electromagnetic wave is passing the transition between two medias with different refractive indices, then the direction of the electromagnetic wave will be changed. The direction change depends on the entrance angle and the difference between the refractive indices. The following theorem describes this relationship.

Scientific law 2.3.1 (See Feynman et al. [2011]:). ***Snell's law*** *states that:*

$$\frac{sin\ \theta_2}{sin\ \theta_1} = \frac{v_2}{v_1} = \frac{n_1}{n_2}$$

where θ_i, v_i and n_i is the corresponding angle, speed of light and the refractive index of the respective medium (see figure 2.9).

The refractive index of air is changing within the atmosphere. Therefore, the ray path through the atmosphere is not a straight line. The lengthening of the ray delay compared to the line of sight delay is denoted as geometric delay δ_g in research publications. It can approximated by the elevation angle θ_e (see [Kouba, 1979] and [Mendes, 1999]). [Kouba, 1979] derive the simple formula

$$\delta_g = \frac{1.92}{\theta_e^2 + 0.6} \tag{2.40}$$

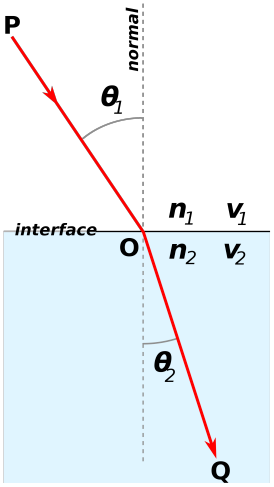

Figure 2.9: Graphic from Wikipedia [uploaded by Alexandrov, 2007]. Refraction of light with $n_2 > n_1$.

while [Mendes, 1999] derive the formula

$$\delta_g = 2.256 \exp\left(\frac{-\theta_e}{2.072}\right). \tag{2.41}$$

The unit is meter and describes the distance an electromagnetic wave would travel in a vacuum within the expected time. Both functions are plotted in Figure 2.10 and show a mismatch. However, it is a matter of fact, that [Kouba, 1979] underestimated the geometric delay effect for small elevation angles and overestimated it for large elevation angles resulting in the observed mismatch [see van der WAL, 1995]. Therefore, the ray bending effect can be neglected for remote sensing applications since the elevation angles are larger than 15 degree commonly. For example, the TanDEM-X satellites have a maximal incident angle of 55 degree which depicts an elevation angle of 35 degree that is mapped to the overestimated 1.6 mm and 1.e-4 mm derived from [Kouba, 1979] and [Mendes, 1999], respectively. The geometric effect in interferograms is even more insignificant, because commonly the incident angles of the master and the slave acquisition are almost the same, so that the geometric delay has shortened itself out of the interferograms. However, the function derived of [Mendes, 1999] indicate that the geometric delay effect is nearly zero (see lower plot in figure 2.10). Correspondingly, the actual ray path is almost equal to the line of sight between the range-azimuth position and the SAR satellite.

Hence, the geometric delay effect does not result in a mis-registration of the interferogram.

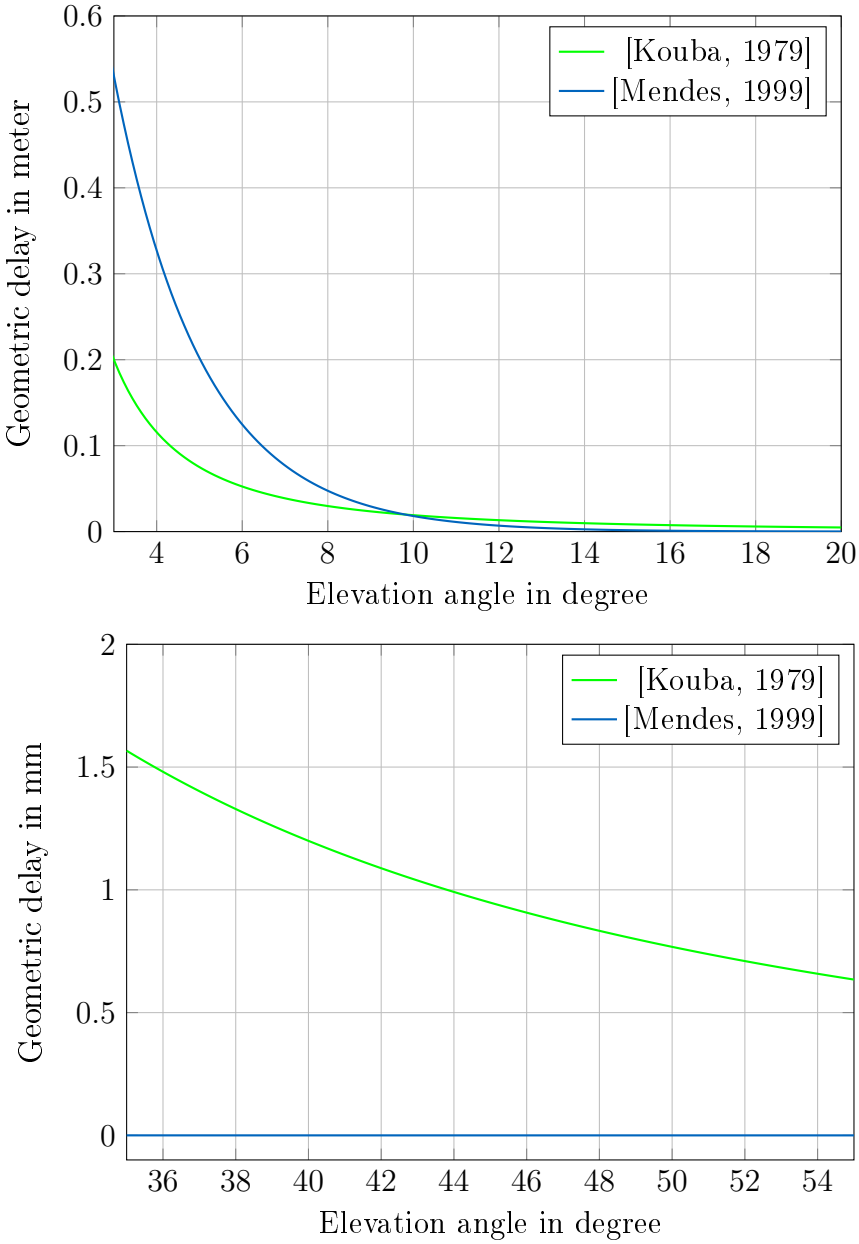

Figure 2.10: The lenghtening of the electromagnetic wave related to the bending effect is plotted depending on the elevation angle.

2.3.2 The delay effect

Now, the delay effect caused by the atmosphere is derived. For the sake of simplicity, the bending effect is neglected and the delay effect is estimated by integrating along the line of sight between the SAR satellite and a target over the refractive index. The following theory is adopted from Davis et al. [1985].

2.3.3 Model description

The delay effect corresponds to the time difference that an electromagnetic wave needs to cross the atmosphere compared to the vacuum

$$\tau_a = \int_{\text{atm}} \frac{1}{v_{\text{atm}}(s)} ds - \int_{\text{vac}} \frac{1}{c} ds = \frac{1}{c} \left(\int_{\text{atm}} n_{\text{atm}}(s) ds - \int_{\text{vac}} 1 ds \right). \tag{2.42}$$

The purpose of the delay estimation is to correct SAR satellite measurements. Therefore, the delay effect is translated into a distance representing the corresponding error

$$\delta_a = \int_{\text{atm}} n_{\text{atm}}(s) ds - \int_{\text{vac}} 1 ds. \tag{2.43}$$

The path through the atmosphere equals the path through the vacuum since the bending effect is neglected. Correspondingly, both integrals can be contracted thus

$$\delta_a = \int_{\text{vac}} n_{\text{atm}}(s) ds - \int_{\text{vac}} 1 ds = \int_{\text{vac}} (n_{\text{atm}}(s) - 1) ds = 10^{-6} \int_{\text{vac}} N_{\text{atm}}(s) ds \tag{2.44}$$

where $N = 10^6 \times (n - 1)$ is a representation of the refractivity.

2.3.4 Atmospheric delay separation

The atmospheric delay is often divided into different parts in literature. These separations follow from the refractivity separations which were derived in sections 2.2.3 and 2.2.4. Practically, the corresponding delays of the separated

terms are calculated and afterwards added. This is formulated by

$$N = N_1 + N_2 \tag{2.45}$$

where N_1, N_2 is the dry / wet or the hydrostatic / non-hydrostatic refractivity separation. In doing so, the corresponding atmospheric delay is separated into

$$\delta_a = \delta_1 + \delta_2 \tag{2.46}$$

where

$$\delta_1 = 10^{-6} \int_{\mathrm{atm}} N_1(s) ds \tag{2.47}$$

$$\delta_2 = 10^{-6} \int_{\mathrm{atm}} N_2(s) ds. \tag{2.48}$$

Chapter 3

Numerical weather prediction

Predicting tomorrow's weather was of interest 100 years ago, and the weather proverb was developed. Numerical weather prediction (NWP) began historically in the 1920s when Richardson produced a 6-hours forecast by using numerical methods by hand [see Lynch, 2008]. A milestone achievement was reached by the Electronic Numerical Integrator and Computer (ENIAC) in Aberdeen Maryland which computed a 24-hours forecast in about 24 hours [see Lynch, 2008]. This was the first time that there was a weather forecast in real time and it was just a matter of time until real and operational forecasts became normality.
However, NWP is also suitable for providing 3-dimensional hindcasts that can be used to estimate the electromagnetic wave delay variations described in section 2. That is why now NWP models are described, most common models listed, their aims and goals described as well as most common initialisation data given.

3.1 Numerical Weather Prediction (NWP)

Vilhelm Bjerknes developed the idea of a weather forecast and described it in the German article [Bjerknes, 1904] that was later translated into English [see Bjerknes, 2009]. Richardson developed the associated algorithm and published it in the book [Richardson, 1922]. Basically, a set of non-linear, partial differential equations have to be solved for a NWP. The reader interested in a comprehensive historical summary is redirected to [Lynch, 2008].

Definition 3.1.1 (basic set of equations)**.** *The basic set of non–linear, partial differential equations for the description of a closed atmospheric system is [see Hoffmann, 1988, Nagel, 1996]*

$$p = \rho R T \qquad \textit{gas law} \tag{3.1}$$

$$\frac{d\rho_d}{dt} = -\nabla \cdot (\rho_d \underline{v}) \qquad \textit{continuity equation for dry air} \tag{3.2}$$

$$\frac{d\rho_w}{dt} = -\nabla \cdot (\rho_w \underline{v}) + S \qquad \textit{continuity equation for moist air} \tag{3.3}$$

$$c_p \frac{dT}{dt} - R\frac{dp}{dt} = Q \qquad \textit{first law of thermodynamics} \tag{3.4}$$

$$\frac{d}{dt}\underline{v} = \frac{1}{\rho}\nabla p - g - 2\underline{\Omega} \times \underline{v} + \underline{F} \qquad \textit{equation of motion.} \tag{3.5}$$

$$\tag{3.6}$$

where

$\underline{v}$	(u, v, w)*velocity vector relative to the earth,*
T	*temperature,*
p	*pressure,*
ρ_d	*density of dry air,*
ρ_w	*density of water vapour,*
$\rho = \rho_d + \rho_w$	*density of moist air,*
$\underline{F}$	*dissipation of momentum,*
S	*water vapour source / sink term,*
Q	*diabatic heating,*
R	*gas constant for moist air,*
c_p	*specific heat at constant pressure,*
$\underline{\Omega}$	*earth angular velocity,*
g	*local gravity acceleration.*

So called "primitive equations" are derived out of the general equations by a number of assumptions to simplify the solution [see Nagel, 1996]. For example, the hydrostatic assumption $\left(\frac{1}{p}\frac{\partial p}{\partial z} + g = 0\right)$ is adequate for a very coarse resolution. In numerical weather prediction, these equations are numerically solved for every time step. The non-linear terms $\rho_{\mathrm{d}}\underline{v}, \rho_{\mathrm{w}}\underline{v}$ and $\frac{1}{\rho}\nabla p$ of

Equations 3.2, 3.3 and 3.5 respectively make the computational effort to derive a solution very expensive. The amount of necessary arithmetic operations are conveniently handled exclusively by a computer, so that only in 1950 the practical benefits could be demonstrated by Von Neumann [see Lynch, 2008].

3.2 Model summary

Several NWP systems exist and are specialized for different tasks. A list of the most common models is given now, but, before, the necessary nomenclature is defined to describe the NWP systems adequately.

3.2.1 Nomenclature

Now, the nomenclature is introduced which is necessary to understand the description of the different models. For this purpose the Glossary of Meteorology of the American Meteorology Society (AMS) [see Glossary of Meteorology of the American Meteorological Society ams] is utilised. First, the AMS published 1959 the Glossary with 7900 terms. The second published version of the year 2000 contained more than 12000 terms. Recently, it was converted into an electronic "Wiki-like" living document.

Scales

NWP is performed in different scales, depending on the application:

- **Synoptic scale:** The area of interest is very large, ranging from several hundred kilometers to several thousand kilometers. In other words, the weather of a continent is predicted and the weather trend is the point of interest. Therefore, mainly high and low pressure systems are predicted.
- **Micro scale or Micrometeorology:** The points of interest are very small scale atmospheric phenomena. So, the area of interest is smaller than one kilometer and forecast duration is less than one day. Therefore, local processes are predicted or investigated. For example, the wind on mountain slopes is a point of interest for paragliders.

- **Mesoscale meteorology:** This time, the point of interest is smaller than the synoptic scale and larger than the micro scale. Hence, the range is from several kilometers to several hundreds of kilometers. Points of interest are thunderstorms, squall lines, fronts, precipitation bands as well as topographically generated weather systems such as mountains waves, sea and land breezes. In other words, the weather of a country is predicted for an average citizen.

Limited-area

Instead of simulating the whole world, just the area of interest is simulated. Hence, the required computational power to calculate the prediction is largely reduced.

Hydrostatic versus non–hydrostatic model

Hydrostatic equilibrium states that the force between pressure and gravity is equal. This assumption works fine if the horizontal scale is large in comparison to the vertical scale which is obvious in the case for synoptic scales. A hydrostatic model uses the hydrostatic equilibrium assumption while a non–hydrostatic model does not.

Sigma coordinate

Topography has a significant influence on the convective flow. Hence, it is essential for a mesoscale or a micro scale model for physically correct simulations. Commonly, this is achieved by using a terrain-following coordinate system like the sigma level system which was introduced by Phillips [1957].

Definition 3.2.1 (sigma level)**.** *The sigma level σ_i of level i is defined by*

$$\sigma_i = \frac{P_i}{P_S} \tag{3.7}$$

where P_i is the pressure at level i and P_S the surface pressure.

State of the art NWPs use generalized versions of the original definition. Nevertheless, the general idea behind a terrain-following coordinate system stays the same (see figure 3.1).

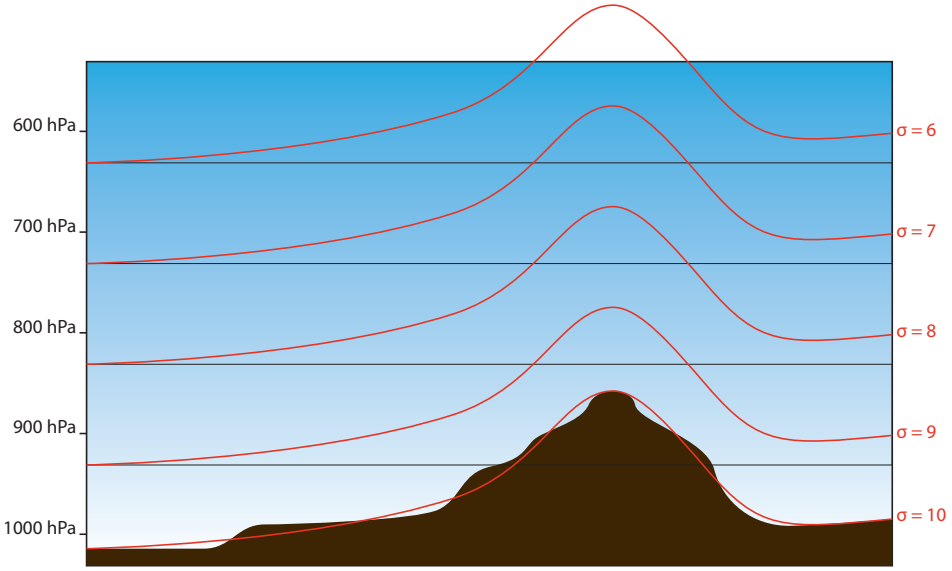

Figure 3.1: Illustration of the terrain following σ coordinate system.

Assimilation

Weather observations are derived from different systems with various characteristics. This means, the quality, the spatial as well as the temporal resolution and the coverage are very different. For example, a weather station provides the surface temperature with high temporal resolution but exclusively at one specific location. In contrast, a weather balloon provides a high vertical resolution at one specific time. However, both kinds of observations are helpful to improve a prediction. It is not applicable to derive the current state of the atmosphere exclusively from the weather observations because of the inhomogeneous distribution of weather observations in space and time. Hence, a NWP model run is pushed towards such observations which is known as data assimilation [see ams].

3.2.2 PSU/NCAR mesoscale model

The PSU/NCAR mesoscale model (MM5) is one of the prominent NWP models in history. It was developed by Penn State University and the National Center for Atmospheric Research NCAR. Major increments were nested domains, nonhydrostatic dynamics and platform independent parallelisation. A

short description is given by [see UCAR, 2018a]:

"The PSU/NCAR mesoscale model (known as MM5) is a limited-area, nonhydrostatic, terrain-following sigma-coordinate model designed to simulate or predict mesoscale atmospheric circulation."

3.2.3 Weather Research and Forecast

An advancement of the MM5 was essential for better research possibilities. For this reason a partnership of NCAR, the National Oceanic and Atmospheric Administration (NOAA), the National Centers for Environmental Prediction (NCEP), the Forecast Systems Laboratory (FSL), the Air Force Weather Agency (AFWA), the Naval Research Laboratory, the University of Oklahoma and the Federal Aviation Administration (FAA) built a new model which is known as the weather research and forecast (WRF) model. The following description was stated on the official website [see UCAR, 2018b]:

"The Weather Research and Forecasting (WRF) Model is a next-generation mesoscale numerical weather prediction system designed for both atmospheric research and operational forecasting applications. It features two dynamical cores, a data assimilation system, and a software architecture supporting parallel computation and system extensibility. The model serves a wide range of meteorological applications across scales from tens of meters to thousands of kilometers."

3.2.4 COSMO

The Consortium for Small-scale Modeling (COSMO) project is a counterpart to WRF and was built by different organizations from Germany, Switzerland, Italy, Greece, Poland, Romania and Russia. The official website describes the model by [see COSMO, 2018]:

"Its general goal is to develop, improve and maintain a non-hydrostatic limited-area atmospheric model, to be used both for operational and for research applications by the members of the consortium."

3.2.5 HIRLAM

The High Resolution Limited Area Model (HIRLAM) was developed within a programme of the European meteorological institutions of Denmark, Estonia, Finland, Iceland, Ireland, Netherlands, Norway, Spain, Sweden, Lituania and France. The aim of this model is described, on the official website, by [see HIRLAM, 2018]:

> "HIRLAM's prime long-term goal is to provide its members with a state-of-the-art operational short and very short range numerical weather prediction system, and the expertise associated with it. The main application for the NWP system is the production of operational weather forecasts for the member services, with particular emphasis on the detection and forecasting of severe weather and services related to public safety."

3.2.6 Model decision

Water vapour, temperature and pressure fields are derived by each NWP model. Therefore, in principle all models can be used to hindcast the APS. However, WRF is the favoured NWP model by the research community. This can be seen in table 3.1. The number of hits on Google Scholar shows a clear lead of the WRF model compared to the other models. This becomes even clearer when one considers that WRF is the successor model of MM5, so the hit counts can be added. Another advantage of WRF is that no administrative effort is necessary to get the source code of it compared to the HIRLAM and the COSMO model. WRF can be downloaded directly while the HIRLAM and the COMSO model require some paperwork in advance.
The unique feature of WRF is that the model focuses on research needs which is explicitly mentioned in the aims and goals of it. Another disadvantage of COSMO and HIRLAM is that the community is limited by their nationality. Therefore and because of the clear leadership in the research community, WRF is the model chosen for these studies.

	Administrative effort	Google Schoolar hits
MM5	free download	7.180
WRF	free download	11.500
COSMO	agreement necessary	2.870
HIRLAM	agreement necessary	3.430

Table 3.1: The effort to get the NWP model source code is different. Some of the models can be downloaded for free, while other models require an agreement to be signed. In addition, the presence in research publications is quite different. The research impact of each model is illustrated by the amount of results found in Google Scholar, where the model name was combined with "NWP" and used for searching.

3.3 WRF details

A detailed description for the WRF setup is now given to highlight the complexity of NWP models, to show the data dependencies and to explain the workflow.

3.3.1 The WRF Preprocessing system (WPS)

The WRF preprocessing system (WPS) uses terrestrial as well as gridded data to derive an initial state for the NWP prediction. Terrestrial data are for example terrain, landuse, and soil types. This information is downloaded once and used for each NWP prediction in the same way. Gridded data are time depending data and must be downloaded for each NWP prediction separately. The WPS system is composed of three programs and the data flow between these programs is illustrated in figure 3.2. The geogrid program defines the model domains, reads a static geographic data set (terrestrial data) and interpolates them spatially. The ungrib program reads the gridded data (meteorological data), decompresses them and converts them into the correct format. The metgrid program uses the output of geogrid and ungrib to interpolate horizontally the meteorological fields. Finally, the so-called real program reads the output of metgrid and interpolates the meteorological fields vertically. The so-called namelist.wps file is the configurations file of geogrid, ungrib and metgrid. A subset of these parameters is for example the number of nesting, the start

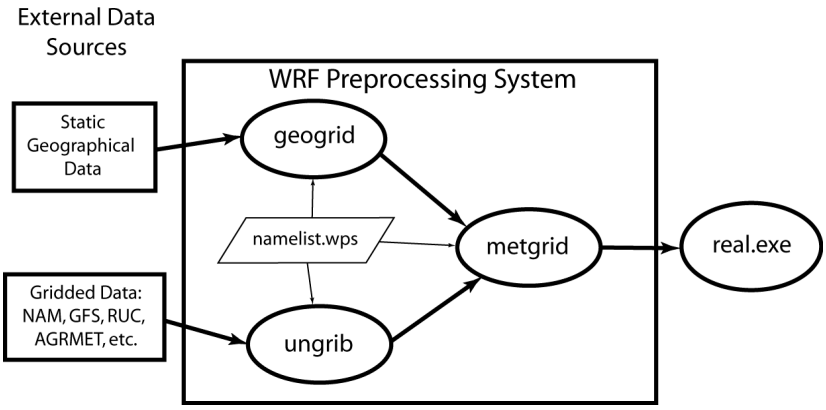

Figure 3.2: The WRF preprocessing system (WPS) is a collection of programs to uncompress data, interpolate data and to combine data sets. This official illustration of the WPS system is from the WRF manual [see Wei Wang et al., 2019].

/ end date, grid ratios, grid positions, grid resolution and the map projection. Most of them are related to geogrid and define the simulated domains. The domain related parameters are described now to provide a better understanding of the simulation and the setup process.

The map projection

The WRF system is a limited area NWP system. This means, only a section of the Earth is simulated. For simplicity, the sphere section of the Earth is mapped onto a plain. This can be done in different ways and the mappings are illustrated in the figure 3.3. The interested reader is directed to the WRF manual [see Wei Wang et al., 2019].

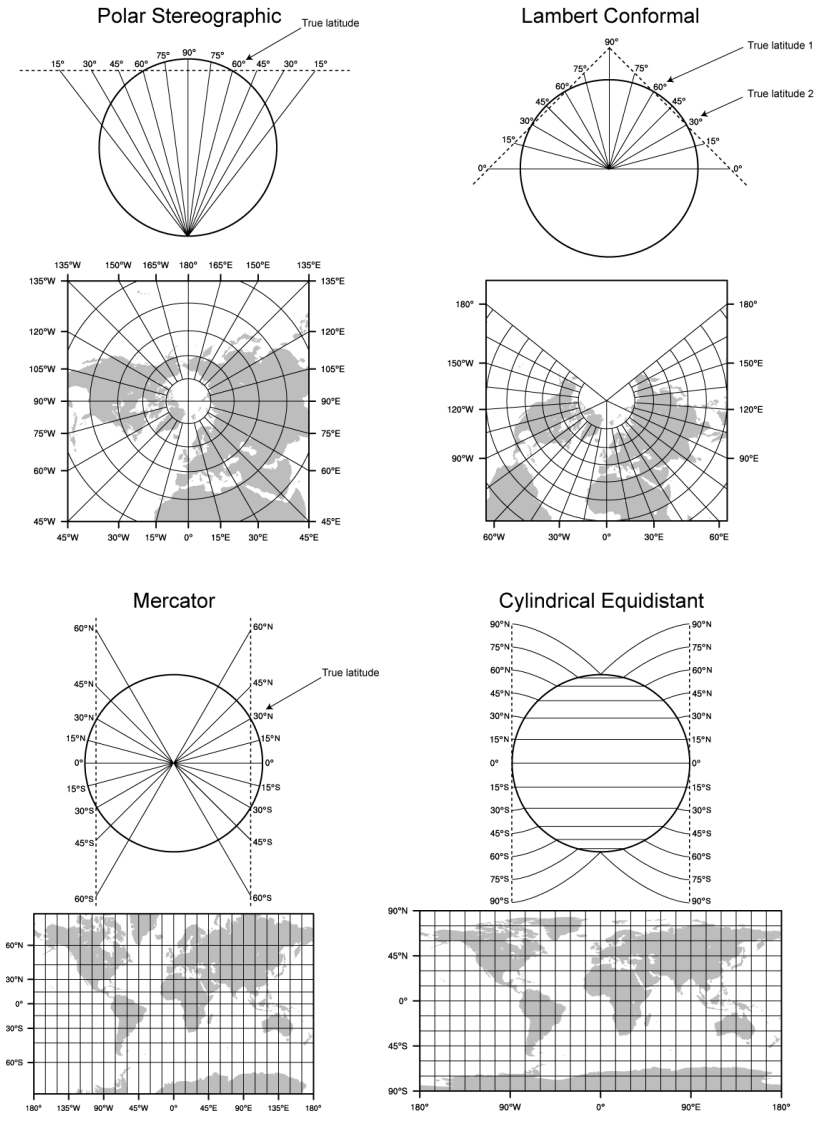

Figure 3.3: Different projections of the Earths surface on a plain are illustrated. This is the official illustration of the WRF manual [see Wei Wang et al., 2019].

The domains

The simulated domains are sampled by a three dimensional grid. The horizontal resolution is equidistant but may be different in the dimensions, i.e. the resolution in the x-direction is not necessarily the same as in the y-direction. The vertical layering is not equidistant and can be defined explicitly or by defining the number of vertical layers. The grid extent multiplied with the resolution equals the size of the simulated area.

The domain nesting

The domain simulation depends on the ambient weather conditions that are not simulated. These ambient conditions are just interpolated in time and space using the initial grid data. Therefore, it is very important to additionally simulate a much larger domain, than the desired domain, to consider the effect of ambient weather conditions. However, commonly it is not possible to simulate the expanded domain with the same resolution as the desired domain, because of the computational effort. Therefore, the desired very high resolution domain is nested inside this much larger so-called parent domain with a coarser resolution. Each simulation is integrated by discrete time steps that depend on the spatial resolution of the domains. This makes it possible to provide good ambient conditions with little additional computational effort. The resolution relation of the nested domains must be an integral number to align the grid cells. The placement definition is illustrated in Figure 3.4.

3.3.2 The WRF Program

The WRF program takes the output of the so-called real program (see section 3.3.1) and computes the actual forecast. The forecast is parameterised by the namelist.input configuration file. The parameter set size is quite large, which is why no detailed description is provided here. However, the most important parameter set categories and settings are listed now.

The time control category

The first parameter category defines the start time, the duration of the prediction, the time frame of the output data, the format of the input and output

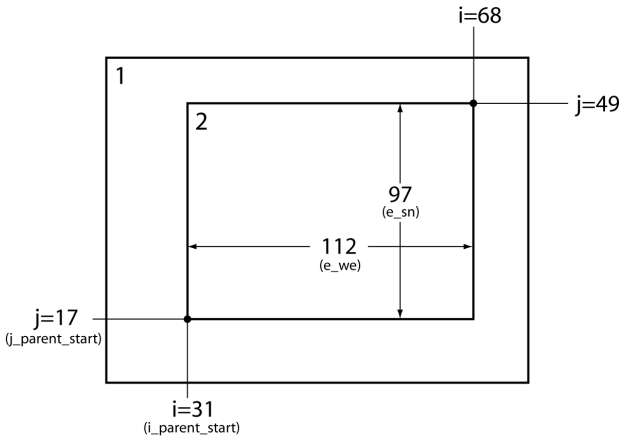

Figure 3.4: Domain two (2) is nested in parent domain one (1). The integral grid ratio number ensures that the bounding box of domain two (2) is aligned to grid cells of domain one(1). This is the official illustration of the WRF manual [see Wei Wang et al., 2019]

as well as the number of input and output files.

The domains category

The forecast is computed iteratively, by using a time step whereby the time step size is related to the horizontal resolution. As a rule of thumb, a factor of six seconds per km resolution is recommended, i.e. a 900 m resolution implicates a time step size of $0.9\text{km} * 6\frac{\text{s}}{\text{km}} = 5.4\text{s}$. If the time step size is too large, then the forecast will fail because the Courant-Friedrichs-Lewy (CFL) condition is violated [see Courant et al., 1928]. This condition takes care, that no information will travel more than one voxel within the grid at each time step. Smaller time steps are valid but increase the computational effort.
It is also possible to use an adaptive time step that is adjusted at each time step so that the CFL condition is not violated. This improves the computational performance and reduces the computational time.
The number of domains, their size, their nestings and positions must be specified again. It is even possible to move nested domains over time. This is especially of interest if some moving extreme weather events should be simulated in very high resolution. However, this is commonly not of interest in this

research area.
The ambient weather conditions flow from parent domains into nested domains. But it is also possible to switch on a feedback option, so that the nested domain has an impact on the parent domain.

The digital filtering initialization technique control category

The initial weather conditions commonly are spatially interpolated from synoptic scale weather data. That is why the weather conditions are physically unbalanced at the beginning of a model run. Hence, the simulation needs time to reach a balanced state. The required time to reach that balanced state is denoted as spin up time in research papers. However, the digital filtering initialization (dfi) technique allows the imbalance at the beginning to be reduced, by integrating back and forward in time and by filtering unrealistic frequencies.

The physics category

This category is the most confusing category. Various physics parameter subcategories must be specified related to radiation processes, surface related processes, boundary layer processes, cumulus physics and micro physics. A reasonable configuration depends on the resolution and is very complex, because the different parameters have influences on each other. However, good starting points are listed in the WRF manual [see Wei Wang et al., 2019] on page 36 for different resolutions. Here, recommended parametrisations define some test cases.

The dynamics category

This category is related to the turbulence / diffusion processes within the atmosphere and specifies also the damping at the top of the model domain which is necessary because of the limited vertical space that models provide. Additionally, the algorithm that solves partial differential equations is defined and parameterised here.

3.4 NWP model initialisation using gridded data

A NWP model uses the current state of the atmosphere to compute the future state. Therefore, each NWP must be initialised. The corresponding input data are obtained from synoptic scale forecast systems. This is necessary, because observations alone are too inhomogeneous in time and space for an initialization. In case of limited area NWPs, the ambient weather of the simulation domain is not simulated. This is a problem, because the ambient weather contributes to the simulated atmosphere. This disadvantage of limited area models is reduced by supporting the simulation with time discrete ambient weather states. Therefore, the synoptic forecasts provide the necessary data and are interpolated in time for simplicity.
A variety of synoptic scale models exists and two well-known centres who provide initialisation data are described now in detail.

3.4.1 ECMWF

The European Centre for Medium-Range Weather Forecasts (ECMWF) was founded in 1975 and has 21 member states and 13 Co-operating states. The main objective is the medium range weather forecast and it therefore produces up to 10 day and beyond predictions [see Thorpe and Adrian, 2013]. It is the acknowledged world leader in this area of expertise [see Thorpe and Adrian, 2013]. For a fair comparison, the World Meteorological Organization (WMO) has defined standards for this rating.
Different types of forecasts are offered e.g. deterministic forecasts, ensemble forecasts, seasonal forecasts and so on. A deterministic forecast is unique and does not provide any information about the uncertainty of the forecast. In contrast, an ensemble forecast consists of several deterministic forecasts while the spread of these forecasts reflects the uncertainty. Seasonal forecasts are not of interest in this research area, because this kind of forecast provides statistical information in time and not in space. The application area of atmospheric delay correction commonly requires data sets of the past. Here, two kinds of datasets must be distinguished. First, analysis datasets and second, reanalysis datasets. Both can be interpreted as a space-time interpolation. However, the quality of analysis datasets varies over time as they are derived

	ERA-interim	ERA5
Period	1979 - now	Current: 1979 - now Future: 1950 - now
Resolution	79 km globally, 60 levels to 0.1 hPa	31 km globally, 137 levels to 0.01 hPa
Frequency	6-hourly analysis, 3-hourly forecast fields	Hourly analysis and forecast fields, 3-hourly for the Ensemble of Data Assimilations

Table 3.2: Comparison between the state of the art initialization data set and the next gen initialization data set from ECMWF.

from different versions of the forecasting system. The versions can differ by their parametrisation, their input data or by the source code. The reanalysis datasets are derived from the same forecasting system and thus guarantee consistent quality. The ERA-interim reanalysis data set covers the time period 1979 to the present and is therefore very useful for the atmospheric delay correction. The ERA5 reanalysis dataset covers the time period 1979 to the present [see ECMWF, 2018b]. However, the covered time period will be extended back to 1950 and will replace the ERA-interim data set in the future. It is expected that the extended ERA5 reanalysis dataset will be available for use by early 2019 [see ECMWF, 2018a]. The main improvements are listed in the table 3.2 [see ECMWF, 2018b]. However, the ungrib program of WPS uses by default the same parameters from the ERA5 as well as from the ERA-interim data set. For completeness, the used parameters are listed in tables 3.3, 3.4 and 3.5.

Name	Short description
Geopotential	This parameter is the gravitational potential energy of a unit mass, at a particular location, relative to mean sea level. It is also the amount of work that would have to be done, against the force of gravity, to lift a unit mass to that location from mean sea level.
Temperature	This parameter is the temperature in the atmosphere.
U component of wind	This parameter is the eastward component of the wind. It is the horizontal speed of air moving towards the east, in metres per second. A negative sign thus indicates air movement towards the west.
V component of wind	This parameter is the northward component of the wind. It is the horizontal speed of air moving towards the north, in metres per second. A negative sign thus indicates air movement towards the south.
Relative humidity	This parameter is the water vapour pressure as a percentage of the value at which the air becomes saturated (the point at which water vapour begins to condense into liquid water or deposition into ice).
10 metre U wind component	This parameter is the eastward component of the 10 m wind. It is the horizontal speed of air moving towards the east, at a height of ten metres above the surface of the Earth, in metres per second.
10 metre V wind component	This parameter is the northward component of the 10 m wind. It is the horizontal speed of air moving towards the north, at a height of ten metres above the surface of the Earth, in metres per second.
2 metre temperature	This parameter is the temperature of air at 2m above the surface of land, sea or in-land waters.

Table 3.3: Listed are the used parameter of the ERA5 and ERA-interim data set. The supplementary lists can be seen in table 3.4 and 3.5. The names and the short descriptions were taken from the parameter database at `https://apps.ecmwf.int/codes/grib/param-db`.

Name	Short description
2 metre dewpoint temperature	This parameter is the temperature to which the air, at 2 metres above the surface of the Earth, would have to be cooled for saturation to occur.
Land-sea mask	This parameter is the proportion of land, as opposed to sea or in-land waters, in a grid box.
Geopotential	This parameter is the gravitational potential energy of a unit mass, at a particular location, relative to mean sea level. It is also the amount of work that would have to be done, against the force of gravity, to lift a unit mass to that location from mean sea level.
Surface pressure	This parameter is the pressure (force per unit area) of the atmosphere on the surface of land, sea and in-land water.
Mean sea level pressure	This parameter is the pressure (force per unit area) of the atmosphere adjusted to the height of mean sea level.
Skin temperature	This parameter is the temperature of the surface of the Earth.
Sea ice area fraction	This parameter is the fraction of a grid box which is covered by sea-ice. Sea-ice can only occur in a grid box which is defined as ocean according to the land sea mask at the resolution being used. Sea-ice cover can also be known as sea-ice fraction or sea-ice concentration.
Sea surface temperature	This parameter is the temperature of sea water near the surface.
Snow density	This parameter is the mass of snow per cubic metre in the snow layer.
Snow depth	This parameter is the depth of snow from the snow-covered area of a grid box.

Table 3.4: This is the first supplementary list of table 3.3.

Name	Short description
Soil temperature level 1	This parameter is the temperature of the soil in layer 1 (0 - 7cm, the surface is at 0cm).
Soil temperature level 2	This parameter is the temperature of the soil in layer 2 (7 - 21cm, the surface is at 0cm).
Soil temperature level 3	This parameter is the temperature of the soil in layer 3 (21 - 72cm, the surface is at 0cm).
Soil temperature level 4	This parameter is the temperature of the soil in layer 4 (72 - 189cm, the surface is at 0cm).
Volumetric soil water layer 1	This parameter is the volume of water in soil layer 1 (0 - 7cm, the surface is at 0cm).
Volumetric soil water layer 2	This parameter is the volume of water in soil layer 2 (7 - 21cm, the surface is at 0cm).
Volumetric soil water layer 3	This parameter is the volume of water in soil layer 3 (21 - 72cm, the surface is at 0cm).
Volumetric soil water layer 4	This parameter is the volume of water in soil layer 4 (72 - 189cm, the surface is at 0cm).

Table 3.5: This is the second supplementary list of table 3.3.

3.4.2 NOAA

The national oceanic and atmospheric administration (NOAA) provides synoptic scale as well as mesoscale forecasts and is therefore the American pendant to ECMWF and a national meteorological institute together. Again, historical reanalysis or analysis data are points of interest. The Climate Forecasts System (CFS) of NOAA provides a reanalysis data set (CFSR) covering the period January 1979 to March 2011 [see NOAA, 2018]. In addition, the CFS Version 2 (CFSv2) model provides analysis data from January 2011 [see NOAA, 2018] to the present and is denoted by CFSv2 Operational Analysis dataset. However, the spatial resolution varies over time for both initialisation data sets.

3.4.3 Resolution limitation for an operational service

NWPs are commonly operated by meteorological institutions of states utilising supercomputers to compute the prediction within a reasonable time. Nowadays, a resolution of 2.8 km is denoted as very high resolution and is used for the operational forecast over Germany for example. In contrast, the resolution of a SAR sensor is much higher and therefore also the resolution of the desired prediction to mitigate atmospheric disturbances. First, the computational complexity and second a benchmark is shown to illustrate the limitations for an operational service for atmospheric disturbance mitigation. The horizontal grid cell count depends quadratically on the resolution. Further, the integration time step that is used to compute the prediction is also related to the horizontal resolution. Correspondingly, the computational complexity is $\mathrm{O}(\frac{1}{r^3})$ with respect to the horizontal resolution r. If the vertical resolution is also adjusted with respect to the horizontal resolution the computational complexity is $\mathrm{O}(\frac{1}{r^4})$. This means, if the spatial resolution of an operational service will be doubled, the computational power must be multiplied by the factor of 8 or 16 respectively, to keep the computational time constant. This is the case, because the computational time scales inversely linearly with the computational power [see Nagel, 1996]. This is not surprising, but also not obvious, since due to synchronisation caused by parallelism, computational overhead is incurred. Fortunately the overhead is negligibly low compared to the NWP calculations. A benchmark demonstrates a reasonable resolution that can be

achieved by using the technologies that are available today. For this purpose, a dual socket server with two AMD Opteron (TM) 6380 2.5 GHz CPUs was used, while each CPU has 32 cores and thus a total of 64 cores were available. With this hardware setting I was able to run a 60 km $\times$ 60 km large test case with a horizontal resolution of 300 m in real time, i.e. a 6 hour forecast by WRF took 6 hours to compute. The interesting thing about this resolution order is that large eddy simulations become meaningful. WRF for this purpose has therefore two parameters that have to be adapted. *diff_ opt* is related to the air mixing due to turbulences while *km_ opt* is related to the method that computes the eddy coefficient. The topography of the underlying terrain has a large influence onto the simulation. Unfortunately, WRF is shipped with a digital elevation model that merely has about 30-arc-seconds resolution which is about 900 m. Therefore, the WRF resolution was about three times higher than the used digital elevation model. To overcome this, the digital elevation model of the Shuttle Radar Topography Mission (SRTM) with a resolution of 90 m was used instead of the conventional digital elevation model of WRF in a second attempt. Unfortunately, all WRF runs even with much smaller time step sizes crashed because the CFL condition was harmed in mountain areas with rough terrain. Correspondingly, it was necessary to smooth the SRTM model to guarantee the CFL condition. However, a closer look into the derived pressure fields revealed unrealistic pressure fluctuations again on rough terrains. These pressure fluctuations have an impact into the mapped APS because the pressure is used to estimate the APS. Finally, I came to the conclusion to use a 900 m resolution instead of a 300 m resolution because the 900 m resolution simulations saves much computational effort, no additional digital elevation model must be included, the WRF predictions are much more robust and predict no obviously unrealistic pressure fluctuations compared to the 300 m simulations.

Chapter 4

State of the art

The APS correction of interferograms can be supported by knowledge about pressure, temperature and water vapour (see for example [Doin et al., 2009, Cong, 2014]) or by other measurements which correlate with the APS (see for example [Delacourt et al., 1998, Wadge et al., 2002]). A detailed description of the error analysis of interferograms is given in [Hanssen, 2001]. The knowledge about pressure, temperature and water vapour fields is derived commonly from meteorological measurements or gridded data can be downloaded which come from global weather models. Unfortunately, the measurements are commonly inhomogeneous in space and time, while the gridded data like ERA5 data provide space homogeneous data but with a very bad resolution and the temporal sampling is large. Measurements that correlate with the APS are also commonly inhomogeneous in space. In contrast, NWP provide high resolution knowledge about pressure, temperature and water vapour that is homogeneous in space and time. The focus of this thesis is on the adaptation of high resolution NWP which is why publications that do not deal with NWP are not further described in detail.

A brief overview of publications related to APS correction utilising high resolution NWP models, is now given. The order of this discussion is chronological with respect to the year of publication.

Chapter 5 provides summaries of the publications of this thesis and is linked to this chapter to embed them into the related publications.

[Hanssen et al., 1999] is a prominent topic related publication. It is not linked to NWP but provides a comprehensive overview of meteorological phenomena that affect interferograms. The mentioned meteorological phenomena are precipitating clouds, a partly precipitating cold front and horizontal convective rolls. It is also suggested that interferograms can be used for forecasting and to study atmospheric dynamics.

[Webley et al., 2004] used the non-hydrostatic three-dimensional (NH3D) model to hindcast the atmospheric state at the Mount Etna in Sicily. The NH3D model does not simulate clouds and precipitation that is why it is not a NWP model. However, the objective of the paper is a comparison of the quality of the predicted APS resulting from different input data. Radiosonde data and NWP output data were used for the initialisation. It is stated that the NWP output data have a clear advantage compared to the radiosonde data because the spatial sampling is much denser and does not depend on the wind that affects radiosonde positions. An ERS-2 interferogram was corrected by using the hindcasted APS resulting from different input sources. By doing so, the radiosonde related residual image shows a slope while the NWP related residual image is not affected by this slope. Therefore, the NWP related predicted APS fits much better to the interferogram compared to the radiosonde related predicted APS.

[Foster et al., 2006] demonstrated to use the MM5 high resolution NWP to hindcast the APS, i.e. to forecast the past APS, and to compensate the disturbing effect in interferograms. The MM5 model was used with a resolution of 3 km and a timing accuracy of 0.5 h with respect to the acquisition time. This means that the hindcast time is about 0.5 hours from the actual acquisition time. By doing so, the APS compensation benefit was only valid for wavelengths larger than 30 km. Unfortunately, it is not known if a higher resolution than 3 km results in better APS compensation for shorter wavelengths than 30 km.

[Perissin et al., 2010] investigated the MM5 NWP model for operational APS correction. The NWP resolution reaches from 1 km down to 500 m in the

surrounding area of Rome. The corrected interferograms were derived from ERS1 and ENVISAT data. The turbulent term could not be well resolved by the MM5 model while topography related water vapour distributions have been found quite in accordance with the interferograms. However, the authors state that the MM5 model was not yet ready for operational APS compensation due to the problem with turbulent water vapour distribution.

[Gong et al., 2010] investigated the performance of the WRF model for APS compensation. The significant influence of the WRF parametrization was revealed. To be exact, the count of vertical model layers and the spin-up time were identified as very important setup properties. Radiosonde data and InSAR data from ENVISAT ASAR were compared to WRF model runs.
A structure function comparison between predicted APS and the InSAR shows a mismatch that could be explained by the diverse resolution of the data sources. That is described later in 5.2. The best possible spin-up time is not provided by the paper but can be found in 5.1.

[Nico et al., 2011] used the WRF model to hindcast the APS for the Pico Island volcano and over Lisbon. It turns out that the spatial lower frequency, starting from several km, can be predicted very well and used to correct the interferograms derived from Envisat-ASAR data. The remaining phase residuals have a Gaussian distribution and it is stated that the standard deviation is close to typical InSAR phase noise. Unfortunately, it is not explained what typical phase noise means, i.e. it could still include atmospheric related residuals.

[Perissin et al., 2011] compared different water vapour estimates against each other, derived from the MEdium Resolution Imaging Spectrometer (MERIS), GPS and MM5. It is stated that the absolute amount of water vapour estimates are similar. However, the accuracy is not good enough to compensate the spatial variability of APSs observed in interferograms. Nevertheless, NWPs seem to be promising to hindcast long wave water vapour distributions that confirms the conclusion of [Nico et al., 2011]. The best short wave performance was derived by GPS. Unfortunately, the GPS technique is based on GPS sta-

tions and is therefore limited by their spatial coverage.

[Pierdicca et al., 2011] compared different ground based (microwave radiometers, radiosoundings, GPS) and spaceborne observations (AMSR-E, MERIS, MODIS) of columnar water vapour with NWP model runs in Central Italy during a 15-day experiment. The integrated precipitate water vapour of the different observations show a significant consistency with the NWP model runs. However, two open issues are mentioned. First, the optimisation of high resolution NWP models for APS compensation is missing. That means, an algorithm is missing, that maximizes the consistency between the hindcast and the interferogram to compensate the APS as much as possible. Second, the assimilation of interferograms into NWP models is missing, too.
In fact, there is a synergy between both issues which is described in section 5.3.

[Gong et al., 2013] investigated the operational High Resolution Rapid Refresh over the Alaska region (HRRR-AK) model performance for APS correction. The model is based on WRF and tuned for the climatic situation present in Alaska. Radiosonde data were compared to model runs. The authors came to the conclusion that the HRRR-AK model shows a better performance in winter compared to the summer time with an factor of two of the residual standard deviation. This is not surprising, since the water vapour content causes the greatest variability of the APS and it is much lower in winter than in summer time. Further, they state that InSAR data can be corrected with residual errors of about 20 mm.

[Foster et al., 2013] investigated the hypothesis, that a final assimilation of weather data improves the APS correction of interferograms. The Meteorological Assimilation Data Ingest System (MADIS) data, GPS delay estimates and water vapour products from the Geostationary Operational Environmental Satellite (GOES) were assimilated to improve the hindcast over the test area around Mount St. Helens (Amboy, Washington, USA). They came to the conclusion, that the APS correction ability can be improved slightly if GPS time delay data are assimilated additionally to MADIS. On the contrary, the APS correction ability becomes worse if GOES satellite data are assimilated

too. This illustrates that the assimilation process is not straight forward. However, the author states it might be possible to significantly improve the APS correction abilities if more spatially dense meteorological data are available.

[Jung et al., 2014] used the WRF model to hindcast the APS and to correct the interferograms for a persistent scatterer analysis of the Kirishima volcano cluster. This made it possible to reduce the height correlated APS effect, the so-called stratification effect. The PSI estimate with the initial APS correction fits much better to a ground truth GPS measurement than the PSI estimate without the initial correction. This demonstrated the practical application of NWP models for APS correction, especially to correct the stratification effect.

[Pichelli et al., 2015] demonstrated that interferograms and Edium Resolution Imaging Spectrometer (MERIS) data can be assimilated by the MM5 model using a 3DVAR technique. Radio soundings, meteorological radar, and raingauge observations were available as ground truth data. The authors came to the conclusion that the weak to moderate precipitation forecast quality can be improved while it had an negative effect on convective cells at the subgrid scale.

[Gong et al., 2015] describes a statistical framework that uses predicted APS to derive statistical properties in order to support the time series analysis. Therefore, the variance of the simulated APS is computed. A conclusion of the paper is, that the predicted APS is usually underestimated by WRF.
The underestimation results from the diverse resolution of the NWP and the interferogram which is described in detail in section 5.2.

Chapter 5

Summary of results

The NWPs provide information about the atmospheric states during SAR acquisitions. This information is then mapped into corresponding delay maps which are then used to correct interferograms derived by SAR data. Some questions and problems arise which are investigated in this work. First, a NWP needs time to build up structure and to overcome initial imbalances. How long this takes and how these imbalances disturb the delay map was unknown. Second, it was unknown whether the predicted delay map frequencies reflect the reality. Third, NWPs have uncertainties which have to be considered.
These topics are addressed in the following full-paper peer reviewed publications

1. [Ulmer and Balss, 2016] *Spin-up time research on the weather research and forecasting model for atmospheric delay mitigations of electromagnetic waves* published in *Journal of Applied Remote Sensing*

2. [Ulmer, 2016] *On the accuracy gain of electromagnetic wave delay predictions derived by the digital filter initialization technique* published in *Journal of Applied Remote Sensing*

3. [Ulmer and Adam, 2017] *Characterisation and improvement of the structure function estimation for application in psi* published in *ISPRS Journal of Photogrammetry and Remote Sensing*

4. [Ulmer and Adam, 2015] *A synergy method to improve ensemble weather predictions and differential sar interferograms* published in *ISPRS Jour-*

and result in this cumulative dissertation. An overview of the findings are given now. However, the interested reader is redirected to the original publication for further details and the methodology used to derive the results.

5.1 Spin-up time and initial imbalances

Two publications investigate the spin-up time and a technique to reach a balanced state of the initialisation faster.

5.1.1 [Ulmer and Balss, 2016] *Spin-up time research on the weather research and forecasting model for atmospheric delay mitigations of electromagnetic waves* published in *Journal of Applied Remote Sensing*

After initialisation, the models need time to derive a physical valid state. This is called the spin-up time, and it affects delay predictions. Figure 5.1 illustrates the derived accuracy related to the forecast duration and shows that the best accuracy is achieved by the 12th forecast hour. This positive impact of a 12-h spin-up time on delay mitigation has been reported in [Ulmer and Balss, 2016]. Hence, four independent experiments are considered, revealing the best accuracy in the case of 12-h predictions and showing the best consistency of spatial frequencies. The results of the four experiments are now presented. The reader interested in a more detailed description of these experiments is referred to [Ulmer and Balss, 2016].

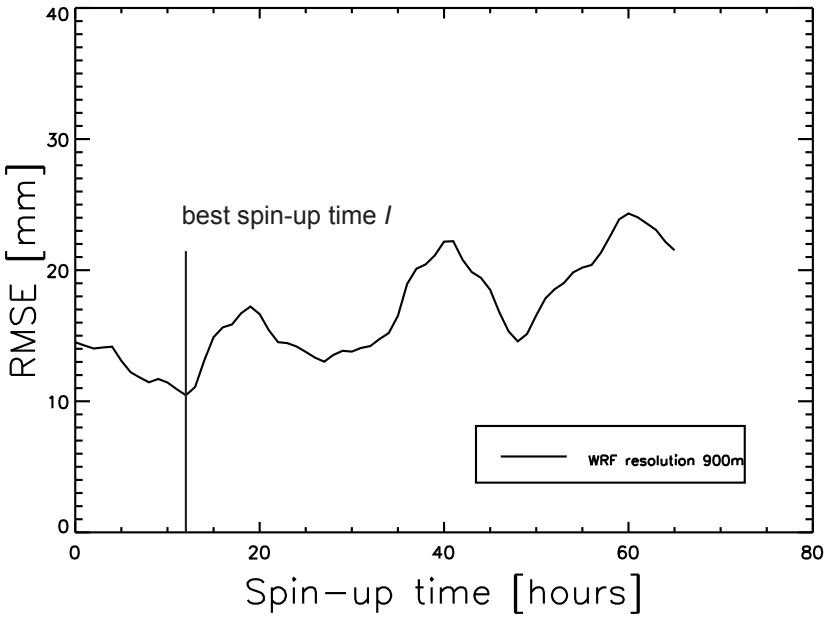

Figure 5.1: This figure shows the derived accuracy as a function of the duration of the prediction. The initialisation weather data form the starting point of the forecast and therefore refer to the zero forecast hour. The best spin-up time is marked by I and reached by the 12 hour forecast time. This means that the best delay reduction is achieved by using initialisation data referring to the 12-hour time before the actual SAR acquisition. A detailed explanation is published in [Ulmer and Balss, 2016].

Global Navigation Satellite System Experiment

First, global positioning system zenith path delay (ZPD) series are compared with model-predicted ZPD series, which reports a 28 % reduction of the root mean squared error. The histogram of the residuals show a Gaussian centered distribution, that is why the RMSE equals the standard deviation of the residuals (see Figure 5.2). However, it is important to mention that the downward trend within the first 12 hours in Figure 5.1 does not come from a time-of-day correlated effect. This is true because the time-of-day-dependent effect, shown in Figure 5.3, indicates an upward trend within the first 12 hours. The observed RMSE trends in Figure 5.3 and 5.1 are both significant with a significance level of 95 %.

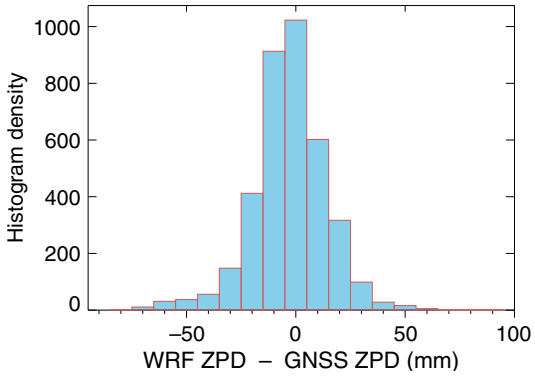

Figure 5.2: This figure shows the residual between the GNSS derived ZPD and the hindcasted ZPD. A detailed explanation is published in [Ulmer and Balss, 2016].

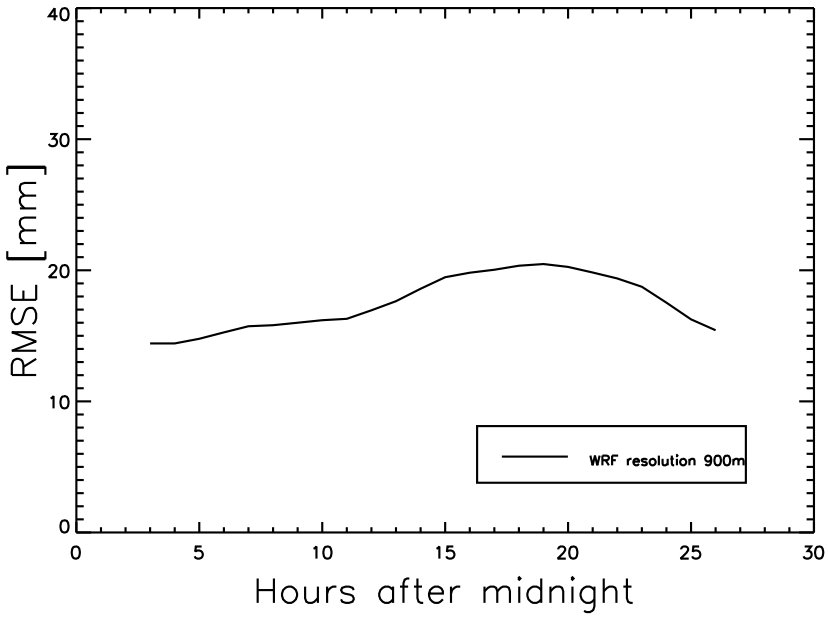

Figure 5.3: This figure shows time-of-day-dependent accuracy. A detailed explanation is published in [Ulmer and Balss, 2016].

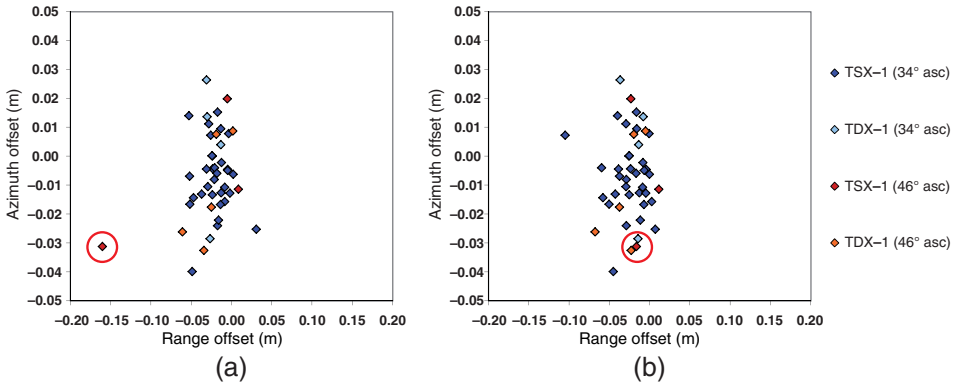

Figure 5.4: Absolute range displacement for (a) the 5-h prediction and (b) the 11-h prediction. A detailed explanation is published in [Ulmer and Balss, 2016].

SAR absolute ranging technique experiment

Second, for the absolute ranging technique, the position of a corner reflector is measured within an SAR image, which is influenced by the atmospheric path delay. For improved estimates of the position of the corner reflector in SAR images, the atmospheric delay is predicted from WRF and is used to correct SAR signals. A more precise prediction of the atmospheric delay is equivalent to a more precise estimate of the corner reflector position.

The SAR absolute ranging technique as an application of the delay prediction reports a 21 % standard deviation decrease of position estimates. Here, the residuals show a bias, whereby this bias remains stable for different forecast durations. The unchanged bias behaviour is expected since the first experiment shows a centered Gaussian distribution. However, this experiment shows an improved outlier correction by using a 11 hour prediction rather than a 5 hour prediction resulting from the fact that WRF predictions within the first 6 hours are too wet [see Jankov et al., 2007]. The range offset, caused by erroneous precipitation is highlighted by the red circle in Figure 5.4 (a) whereby this outlier is corrected by using a 11 hour prediction shown in Figure 5.4 (b).

Spatial frequencies experiment

Third, a comparison of spatial frequencies between APS predictions and interferograms shows a closer consistency using a 12-h rather than a 6-h spin-up time. An example of an interferogram and the corresponding APS prediction is shown in Figure 5.5. The interferogram and the predicted APS are transformed into the wavelet domain the spatial frequencies to be analysed. Different wavelet domains provide different spatial frequencies and act like a filter in our approach. Frequencies below the NWP resolution are filtered out in order to keep only those frequencies for comparison that are resolved by the interferogram as well as by the predictions. The log variances of the wavelet domain coefficients are used to derive scatter plots shown in Figure 5.6. The 6-h prediction shows a structural over- or underestimation of the variances because the dots lie beneath or on top of the red line. This is not the case for the 12-h prediction, which illustrates the advantage of the longer spin-up time and is consistent with the kinetic energy spectra investigation [see Skamarock, 2004]. Additionally, the linear relationship is close to 1 in both cases but slightly better for the 12-h predictions.

APS mitigation experiment

Fourth, APS mitigation in interferograms as an application of APS prediction is twice as good with respect to the 12-h spin-up time as with the 6-h spin-up time. Therefore, the same interferograms of the last experiment were corrected by the predicted APS of the 6-h and the 12-h prediction. The covered area is east of Mexico City, and it is known that this area has no linear subsidence [see Chaussard et al., 2014]. The interferometric digital elevation model error signal is related to the spatial baseline, which varies from 8.1 to 45.3 m. Consequently, the standard deviations of the interferograms Φ_i with small baselines are mainly related to the APS. However, the predicted APS of the NWP has a much lower spatial frequency than the digital elevation model error. Therefore, the derived signal reduction is independent of the high-frequency digital elevation model error, which is present in interferograms with large spatial baselines. The standard deviations of the residuals $\hat{\Phi}_i^6$ and $\hat{\Phi}_i^{12}$ are presented in Table 5.1. On average, the APS mitigation reduces the APS disturbance by

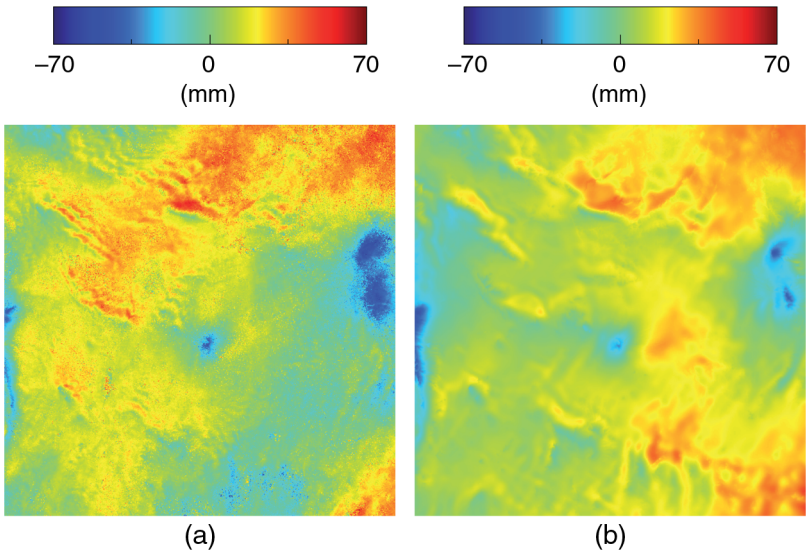

Figure 5.5: (a) The interferogram of the acquisitions December 2, 2014, and November 8, 2014, east of Mexico City and (b) the corresponding predicted APS using a 12-h spin-up time. A detailed explanation is published in [Ulmer and Balss, 2016].

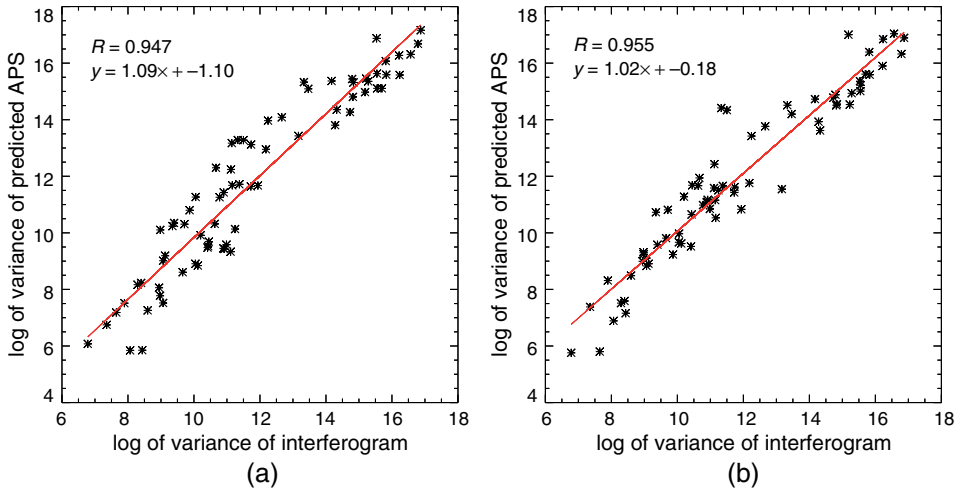

Figure 5.6: Scatterplot of log variances of wavelet domains between interferograms and simulated APS with (a) 6-h spin-up (b) and 12-h spin-up. A detailed explanation is published in [Ulmer and Balss, 2016].

about 9 % and 18 % with respect to the 6-h and 12-h spin-up times, respectively. The accuracy gain results from the closer frequency consistency, which was revealed by the last experiment.

Φ_i	$\hat{\Phi}_i^6$	$\hat{\Phi}_i^{12}$	spatial baseline
16.6	14.6	10.6	17.6
14.7	15.4	13.9	9.1
12.0	10.7	8.6	45.3
16.9	14.3	16.5	8.1

Table 5.1: Standard deviation in mm of the interferograms Φ_i, the residuals after APS correction derived by 6 hour $\hat{\Phi}_i^6$ and 12 hour $\hat{\Phi}_i^{12}$ predictions and the related spatial baselines of the interferograms in m.

5.1.2 [Ulmer, 2016] *On the accuracy gain of electromagnetic wave delay predictions derived by the digital filter initialization technique* published in *Journal of Applied Remote Sensing*

After initialisation, the model needs time to reach a balanced state, such that first prediction steps contain errors. The imbalance causes false predicted precipitation, which then affects the water vapour distribution resulting in an erroneous APS map. The digital filtering initialisation (DFI) technique reduces these imbalances and the ZPD prediction disturbances, respectively. The DFI technique reduces this undesirable behaviour by integrating backward and/or forward in time, and removes nonphysical high frequencies by using a digital filter [see Huang et al., 2007]. In [Ulmer, 2016] the accuracy gain for ZPD predictions is reported, which is achieved by this technique. For the accuracy gain investigation, predicted ZPD time series of the WRF model with and without DFI are compared against Global Navigation Satellite System (GNSS)-derived time series from 233 GNSS stations mainly located in Germany. Two conclusions are drawn: First, the experiment confirms that the DFI technique improves the precipitation forecast. Second, the corresponding accuracy gain, i.e., the bias of ZPD predictions, improves by about 13 %, but

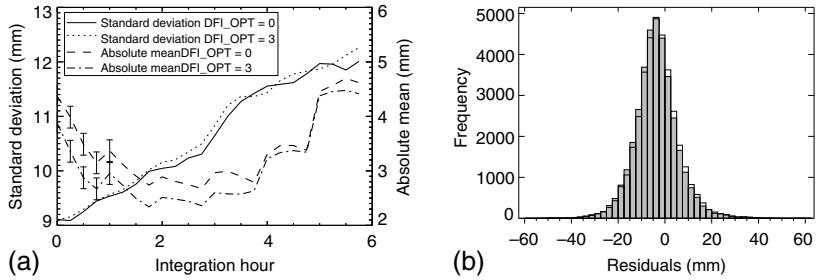

Figure 5.7: The mean and standard deviation of the residual between the predicted ZPD and the GNSS derived ZPD with respect to the integration hour and (b) the histogram of them for the first hour. A detailed explanation is published in [Ulmer, 2016].

the accuracy gain is only valid for the first 4 h of the prediction. The bias correction can be seen in Figure 5.7 (a) where the absolute mean function related to the DFI technique is closer to zero compared to its counterpart related to the common initialisation. However, the biases are very close together after the fourth hour of the prediction. Another illustration of the bias correction is shown in Figure 5.7 (b), where the histograms of the residuals relating to the first 4 hours of the forecast are shown. The associated centre of mass of the DFI technique is closer to zero than with the common initialisation. The bias correction results from a better PWV prediction. This is true because the histogram shapes of the PWV differences (Figure 5.8 (a)) and the ZPD differences (Figure 5.8 (c)), derived from the DFI and the common initialisation, have the same shape. In contrast, the histogram of pressure differences show a symmetry that is presented in Figure 5.8 (b).

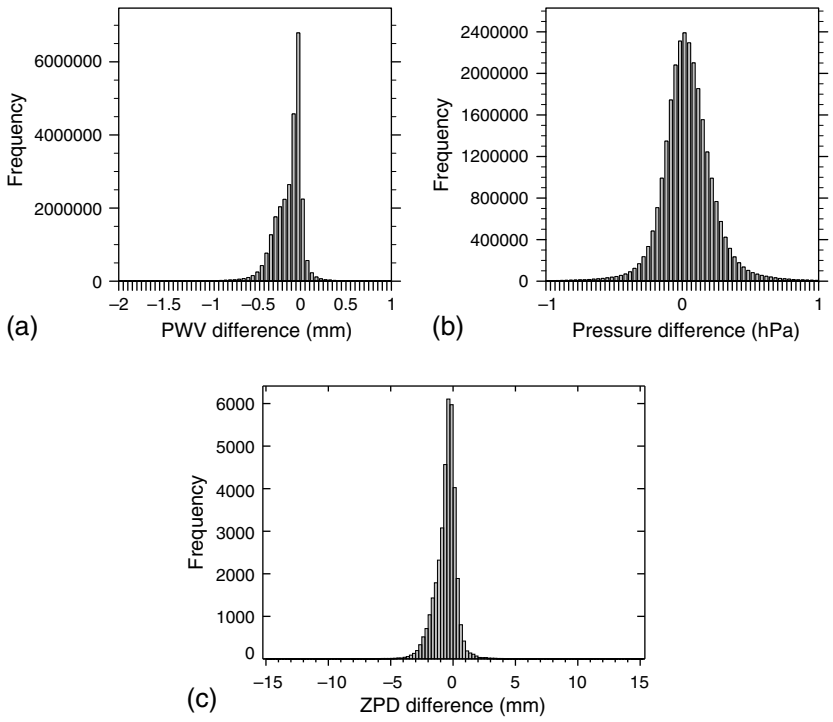

Figure 5.8: Difference histogram between the common initialisation and the DFI predictions with respect to (a) PWV, (b) pressure, and (c) ZPD. A detailed explanation is published in [Ulmer, 2016].

5.2 [Ulmer and Adam, 2017] *Characterisation and improvement of the structure function estimation for application in psi* published in *ISPRS Journal of Photogrammetry and Remote Sensing*

The structure function (variogram) estimated on the InSAR data and on the NWP data is a statistical characteristic which is very useful in the processing and the analysis of the data. For example, the structure function (typically the semivariogram) estimated on InSAR data is fundamental for the Kriging interpolation of the atmospheric phase screen (APS) based on irregular PSI estimates. The required parameters are the nugget, the range and the slope of the structure function. The practical implementation has shown that the NWP predicted structure function and the InSAR estimated structure function based on the conventional semivariogram equation do not match as expected. Possible straightforward explanations are wrongly estimated APSs due to an insufficient number of interferograms or hindcasts that fail to capture the turbulent water vapour signal. However, in [Ulmer and Adam, 2017] the effects of noise in interferograms and truncated resolution of the NWP on the structure function estimation, resulting in the observed mismatch, is explained. Noise causes a flattening of the derived function for short ranges. This can be seen by comparing the dashed lines with the solid lines in Figure 5.9 (a). The truncated resolution however resulting in a changed slope. This can be seen in Figure 5.9 (b) by comparing the dashed lines with the solid lines. To clarify, the truncated resolution is the resolution of the NWP compared to the much higher resolution of interferograms. It is clear that no NWP can capture the turbulent water vapour signal at subgrid scales. However, the mismatch of the structure function can be easily misinterpreted that no frequencies at all of the NWP can capture the water vapour signal correctly. In order to avoid the mismatch, an alternative implementation based on wavelets is suggested and demonstrated using real Sentinel-1 data. The advantage of the proposed technique is illustrated in Figure 5.10. It compares the variance estimations

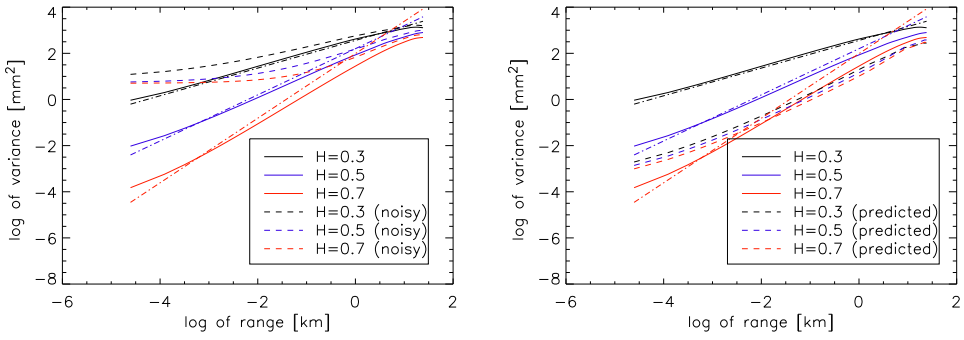

Figure 5.9: Solid lines are the structure functions estimated from noise free fractals. Dashed lines illustrate the effect on the structure function estimation caused by (a) additional noise and (b) lower resolution hindcasts. Since APSs are characterised by the Hurst parameter H = 0.7 [see Hanssen, 2001], the corresponding lines are bold and red. Theoretical straight lines (- · -) representing a Hurst exponent are plotted in the corresponding colour. A detailed explanation is published in [Ulmer and Adam, 2017].

of the fractal and the noisy / truncated resolution fractal. The affine relationships $y = 0.94x + 0.59$ and $y = 1.16x + 2.9$ of scatterplots in Figure 5.10 are close to the perfect affine relationship $y = x$. Further, the very good correlations $R = 0.998$ and $R = 0.999$ between the variance estimations of nearly one illustrate the variance estimation independence in the presence of noise and truncated resolution. Application of the proposed structure function alternative based on NWP data are the master selection, the estimation of the effective NWP data resolution, and a statistical consistency check of the estimated InSAR APS. The comparison between real Sentinel-1 data and hindcasted APS maps is shown in Figure 5.11. Figure 5.11 (a) demonstrates that the water vapour signal can be captured by WRF at frequencies that are covered by the WRF resolution. The effective resolution can be derived by analyzing Figure 5.11 (b). The first three wavelet domains causing a bend in this scatterplot whereas the break of slope defines the effective resolution that is in agreement with the used WRF resolution of 900 m.

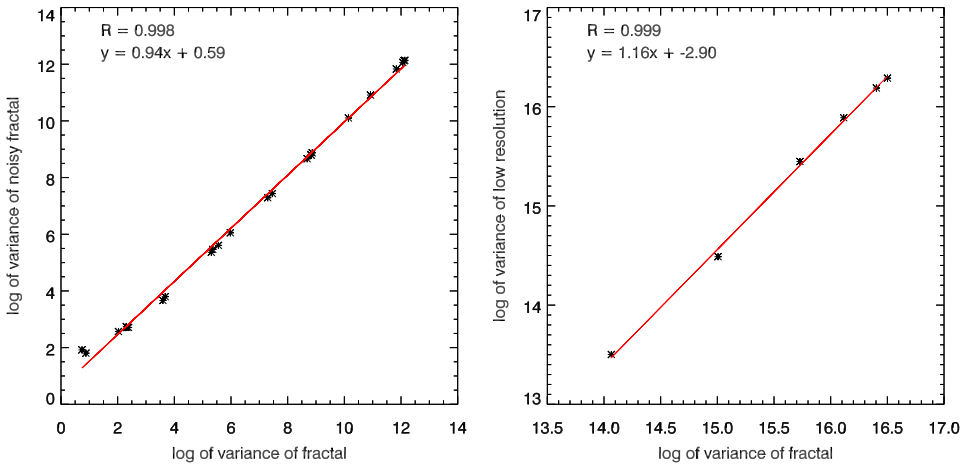

(a) (b)

Figure 5.10: Scatter plots of the wavelet domain variances between the fractal, (a) the noisy fractal and (b) the coarse prediction. A biasing effect would result in a bent curve while perfect matching estimates would result in an affine relationship y = x and correlation coefficient R = 1. A detailed explanation is published in [Ulmer and Adam, 2017].

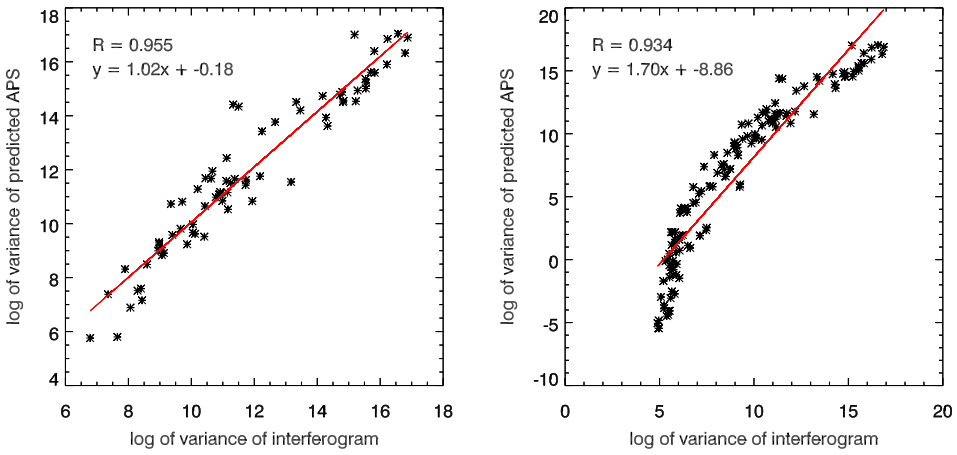

(a) (b)

Figure 5.11: Scatterplot of the sample variances from different wavelet domains between the observed interferograms APSs and the hindcast APSs. (a) First three wavelet domains are skipped; (b) all wavelet domains are considered. A detailed explanation is published in [Ulmer and Adam, 2017].

5.3 [Ulmer and Adam, 2015] *A synergy method to improve ensemble weather predictions and differential sar interferograms* published in *ISPRS Journal of Photogrammetry and Remote Sensing*

NWPs are solutions of partial differential equations which never can be precise due to model or initialisation uncertainties. In order to deal with the chaotic nature of the solutions, ensembles of predictions are computed, e.g. also in climate models. From a stochastic point of view, the ensemble mean is the expected prediction, if all ensemble members have an equal likelihood. This corresponds to the typical assumption that all ensemble members are physically correct solutions of the set of partial differential equations and that all ensemble member initialisations are equally likely. DInSAR allows adding to this knowledge. Observations of refractivity can now be utilised to check the likelihood of a solution and to weight the respective ensemble member to estimate a better expected prediction.

The synergy between ensemble weather predictions and differential interferometric atmospheric correction is shown in [Ulmer and Adam, 2015]. A new method is demonstrated first to compensate better for the atmospheric effect in DInSAR and second to estimate an improved numerical weather prediction (NWP) ensemble mean. Practically, a least squares fit of predicted atmospheric effects with respect to a differential interferogram is computed. The coefficients of this fit are interpreted as likelihoods and used as weights for the weighted ensemble mean. Finally, the derived weighted prediction has minimal expected quadratic errors which is a better solution compared to the straightforward best-fitting ensemble member. Furthermore, we propose an extension of the algorithm which avoids the systematic bias caused by deformations. It makes this technique suitable for time series analysis, e.g. persistent scatterer interferometry (PSI). We validate the algorithm using the well known Netherlands-DInSAR test case (see Figure 5.12 and corresponding DInSAR in Figure 5.13) and first show that the atmospheric compensation improves by

	real interferogram	real interferogram + deformation
uncompensated APS	18.01	
blind NWP	15.72	
unweighted ensemble	16.04	
single best-fitting	13.09	13.09
weighted ensemble	9.83	10.09
weighted ensemble (relaxed to ≈ 1)	9.04	9.36
weighted ensemble (without constraint)	8.34	8.85

Table 5.2: Root mean squared error in [mm] of non-compensated APS.

nearly 40 % compared to the straightforward technique. A comparison of the residual APS compensations root mean squared errors can be seen in Table 5.2. The rows list different competing techniques while the columns define two scenarios of a DInSAR without and with artificial deformation respectively. The weighted ensemble techniques result always in the lowest residual error that can be seen by comparing the rows. The artificial deformation that was added to the DInSAR does not disturb the compensation a lot and that can be seen by comparing the columns. Second, we compare our results with independent sea level pressure data. In our test case, the mean squared error is reduced by 29 % compared to the averaged ensemble members with equal weights. The derived competing pressure results are shown in Figure 5.14. Figure 5.14 (a) has much more structure than Figure 5.14 (b) because the unweighted ensemble blurs out higher spatial frequencies. An application demonstration using actual Sentinel-1 data and a typical test site with significant subsidence (Mexico City) completes the paper. The Mexico City subsidence, highlighted by the black circle in Figure 5.15 (b), of 25 mm/month [see Chaussard et al., 2014] is better estimated in Figure 5.15 (b) compared to 5.15 (a). Additionally, the vertical stratification effect, i.e. the APS correlation with height is now completely mitigated (highlighted in Figure 5.15 (a)).

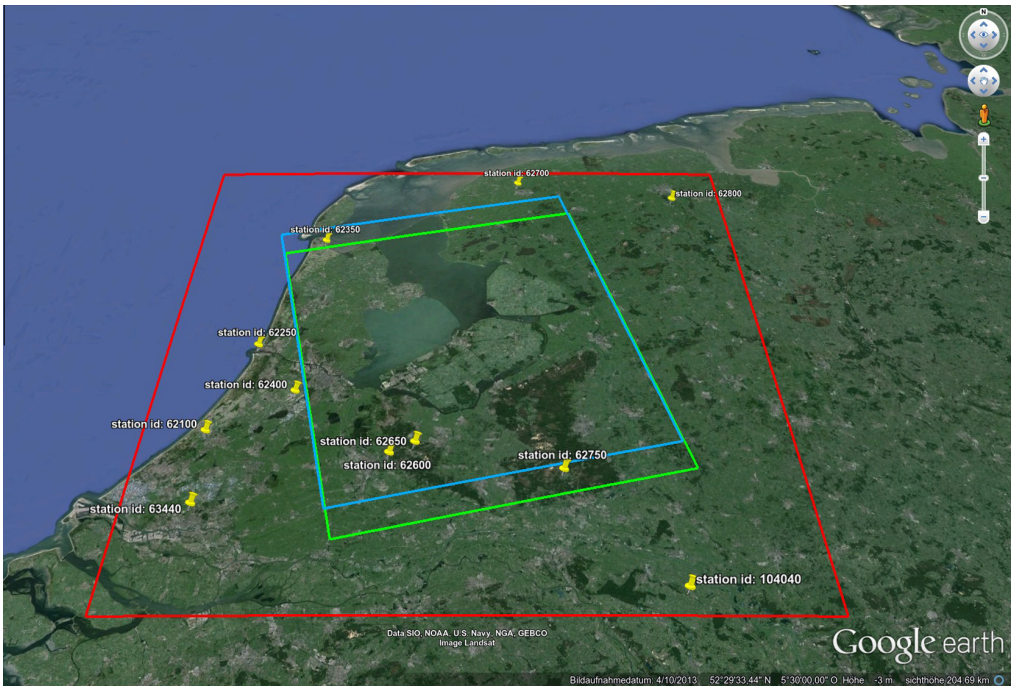

Figure 5.12: Illustration of test site. The outer rectangle is the finest domain of NWP while the inner rectangles illustrate the SAR coverage of the acquisitions on 3rd and 4th October 1995. Weather stations are illustrated by yellow pins. The DInSAR image corresponds to the intersection of inner rectangles. A detailed explanation is published in [Ulmer and Adam, 2015].

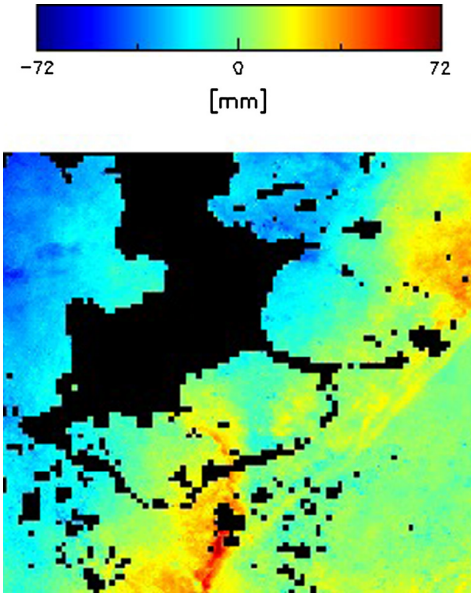

Figure 5.13: DInSAR of 3rd and 4th October 1995 at 21:41 UTC is shown. A detailed explanation is published in [Ulmer and Adam, 2015].

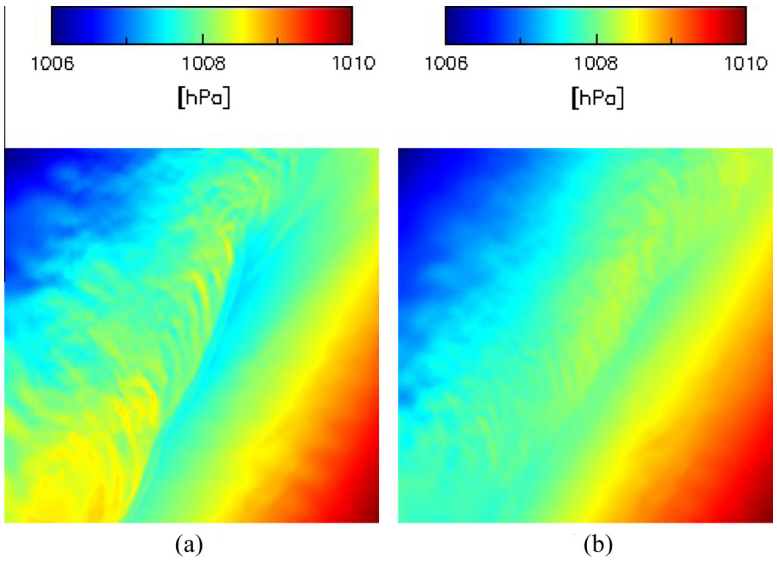

Figure 5.14: Surface pressure prediction at October 4th of (a) WEM (b) unweighted ensemble at 21:40 UTC. A detailed explanation is published in [Ulmer and Adam, 2015].

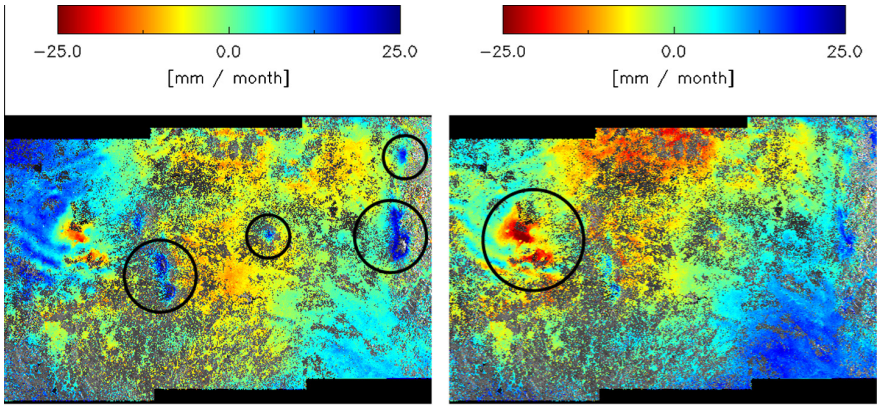

Figure 5.15: Linear deformation estimations of (a) uncompensated interferograms and (b) compensated interferograms. A detailed explanation is published in [Ulmer and Adam, 2015].

Chapter 6

Discussion

The findings of the author's publications are now combined, with the common central goal to mitigate the APS as much as possible and keeping the computational effort as low as possible. [Ulmer, 2016] reports that the digital filter initialization technique reduces falsely predicted precipitation within the first 4 hours of the prediction while [Ulmer and Balss, 2016] reports that the best accuracy is reached after 12 hour spin-up time. This means that the time frame of the DFI improvement and the optimal accuracy related read out time frame do not overlap which is illustrated by the yellow and the blue rectangle in Figure 6.1. Correspondingly, the additional effort for the application of the digital filter initialization technique is not justified. The initialization data have a temporal sampling of 6 hour commonly. This is illustrated by the two possible read out marks in Figure 6.1. Therefore, it is not always possible to use a 12 hour prediction. Hence, I recommend a setting that the prediction time lies between 6-12 hour to reach a good accuracy while keeping the computational cost low. That is illustrated by the green time frame in Figure 6.1. However, if computational power is available, then the blue illustrated time frame in Figure 6.1 should be used.

Ensemble predictions are quite computationally expensive because a couple of 6-12 or 9-15 hour predictions have to be computed. Different ensemble prediction settings are possible. First, different physical parametrizations of the WRF model are possible. Second, different initialization data sets can be used. Third, initialization data sets can be slightly modified. Last but not least, the timing of a prediction can be also seen as uncertain because of wrongly ini-

tialized convection. The ensemble members of the first approach describe the uncertainties with respect to the parameter setting. The ensemble members of the other approaches represent the uncertainties with respect to the initialization data. The combination of all approaches cover the overall uncertainty and result in a best weighted ensemble mean that fits as well as possible the observed APS. The computational cost to predict all these ensembles is quite high, but the benefit is large. In [Ulmer and Adam, 2015] it is shown that the required number of scenes can be reduced by 70 % to reach an accuracy of 1 mm, over an arbitrary scale, for the deformation estimation, by using exclusively ensemble members of the first and the last approach. However, if the computational cost is too large the NWP resolution can be reduced, e.g. by omitting the nested domain with the highest resolution, by changing the resolution ratios of the nested domains or by redefining the resolution of the outer domain. This is recommended, because of the complexity of the NWP which is at least $O(\frac{1}{r^3})$ and the fact that most of the APS power is related to low frequencies [see Ulmer and Adam, 2017].

If the recommended setting is applied, most of the energy of the stratification effect, low frequency APS and other APS patterns related to well predictable atmospheric conditions is mitigated. However, residual APS is still present due to the chaotic nature of convection and needs to be reduced by using time series analysis of interferometric images. This analysis can be supported by adding the statistical characterization of the residual APS. The APS characterisation can be derived from a single NWP as it is shown in [Ulmer and Adam, 2017]. Correspondingly, it is recommended, that the ensemble members are computed in a lower resolution while keeping the resolution for a single prediction high.

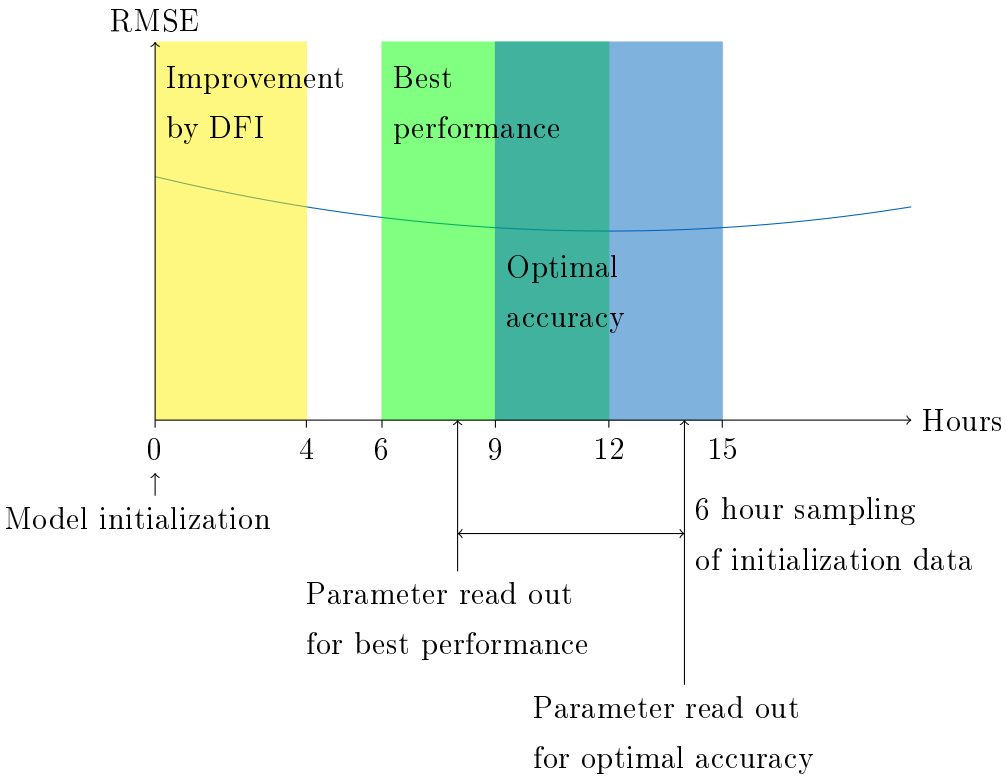

Figure 6.1: This figure illustrates the different findings of the author's publications. The yellow time frame illustrates the time where the DFI technique improves the forecast. The green time frame illustrates the best trade-off between computational effort and accuracy. The blue time frame illustrates the time frame that provides the best accuracy.

Chapter 7

Outlook

Currently, a lot of interesting developments are in progress that have the ability to improve the APS correction further. First, the computational power is becoming larger and new techniques like GPU computations are implemented for NWP. This allows the computational time to be reduced, the resolution of the NWP to be improved or the number of ensemble members to be enlarged. Second, new grid types are investigated for NWP. Commonly, the grids are based on equally sized rectangles. Alternatives are for example hexagonal or triangle based grids with varying sizes of grid elements. This is especially of interest to adapt the resolution depending on the surface complexity or on the area of interest. However, some problems must be solved to become applicable. So the CFL criterion must remain fulfilled, which is why the time step size depends on the highest resolution in the grid, which makes it unpractical for large grids. Third, the temporal resolution of input data may become better in future. This allows the spin up time to be better adjusted, the quality to be improved and the computational effort to be reduced. Last but not least, new remote sensing techniques allow information to be derived that have the ability to improve the NWP quality. For example, the Aeolus mission provides wind profiles that can be assimilated by weather forecasts. This is especially of interest because convection distributes water wapour and that is why it has a direct impact on the derived APS quality.

Chapter 8

Conclusion

The combination of NWPs with interferograms is useful for both sides: First, the interferograms can be corrected by using NWPs. Second, the NWPs can be improved by using interferograms. The correction of interferograms is supported by two approaches. First, by computing the best fitting APS to the interferogram and by subtracting the fitted APS from the interferogram. Second, by using the statistical characterization of an APS derived from a single very high resolution NWP. The NWP resolution of the first approach can be reduced to save computational power or to predict more ensemble members for the least square fit. However, each prediction shall cover at least 6 hours, but preferable 12 hours, to reach a balanced state and to build up realistic structures.

Bibliography

URL http://glossary.ametsoc.org.

Oleg Alexandrov, 2007. URL https://commons.wikimedia.org/wiki/File:Snells_law2.svg.

B.R. Bean and E.J. Dutton. Radio meteorology. National Berau of Standarts, 1966.

Benji9072. ball-and-stick model of co2: carbon dioxide, 2010. URL https://commons.wikimedia.org/wiki/File:Carbon_dioxide_structure.png.

V. Bjerknes. Das problem der wettervorhersage, betrachtet vom standpunkte der mechanic und der physik. Meteorolgische Zeitschrift, 1904.

Vilhelm Bjerknes. The problem of weather prediction, considered from the viewpoints of mechanics and physics. Meteorologische Zeitschrift, 18(6): 663–667, 12 2009. doi: 10.1127/0941-2948/2009/416. URL http://dx.doi.org/10.1127/0941-2948/2009/416.

Estelle Chaussard, Shimon Wdowinski, Enrique Cabral-Cano, and Falk Amelung. Land subsidence in central mexico detected by alos insar time-series. Remote Sensing of Environment, 140:94 – 106, 2014. ISSN 0034-4257. doi: https://doi.org/10.1016/j.rse.2013.08.038. URL http://www.sciencedirect.com/science/article/pii/S0034425713002964.

Xiaoying Cong. SAR Interferometry for Volcano Monitoring: 3D-PSI Analysis and Mitigation of Atmospheric Refractivity. Dissertation, Technische Universität München, München, 2014.

COSMO. http://www.cosmo-model.org/, 4 2018. URL http://www.webcitation.org/6yV5tfKMf.

R. Courant, K. Friedrichs, and H. Lewy. Über die partiellen Differenzengleichungen der mathematischen Physik. Mathematische Annalen, 100:32–74, 1928. doi: 10.1007/BF01448839.

B. D. Cullity and C. D. Graham. Introduction to Magnetic Materials. Wiley-IEEE Press, 2 edition, 2008. ISBN 0471477419, 9780471477419.

J. L. Davis, T. A. Herring, I. I. Shapiro, A. E. E. Rogers, and G. Elgered. Geodesy by radio interfereometry: Effects of atmospheric modeling errors on estimates of baseline length. Radio Science, 20:1593–1607, 1985.

C. Delacourt, P. Briole, and J. A. Achache. Tropospheric corrections of sar interferograms with strong topography. application to etna. Geophysical Research Letters, 25(15):2849–2852, 1998. doi: 10.1029/98GL02112. URL https://agupubs.onlinelibrary.wiley.com/doi/abs/10.1029/98GL02112.

M.-P. Doin, C. Lasserre, G. Peltzer, O. Cavalié, and C. Doubre. Corrections of stratified tropospheric delays in SAR interferometry: Validation with global atmospheric models. Journal of Applied Geophysics, 69:35–50, September 2009. doi: 10.1016/j.jappgeo.2009.03.010.

ECMWF. https://www.ecmwf.int/en/forecasts/datasets/reanalysis-datasets/era5, 4 2018a. URL http://www.webcitation.org/6yZz87xL7.

ECMWF. https://www.ecmwf.int/en/newsletter/147/news/era5-reanalysis-production, 4 2018b. URL http://www.webcitation.org/6yfiJRlkb.

R.P. Feynman, R.B. Leighton, and M. Sands. The Feynman Lectures on Physics, Vol. II: The New Millennium Edition: Mainly Electromagnetism and Matter. Feynman Lectures on Physics. Basic Books, 2011. ISBN 9780465024940. URL https://books.google.de/books?id=hlRhwGK40fgC.

J. Foster, B. Brooks, T. Cherubini, C. Shacat, S. Businger, and C. L. Werner. Mitigating atmospheric noise for insar using a high resolution weather model. Geophysical Research Letters, 33(16), 2006. doi: 10.1029/2006GL026781. URL https://agupubs.onlinelibrary.wiley.com/doi/abs/10.1029/2006GL026781.

James Foster, John Kealy, Tiziana Cherubini, Steven Businger, Zhong Lu, and Michael Murphy. The utility of atmospheric analyses for the mitigation of artifacts in insar. Journal of Geophysical Research: Solid Earth, 118(2):748–758, 2013. doi: 10.1002/jgrb.50093. URL https://agupubs.onlinelibrary.wiley.com/doi/abs/10.1002/jgrb.50093.

W. Gong, F. Meyer, P. W. Webley, D. Morton, and S. Liu. Performance analysis of atmospheric correction in insar data based on the weather research and forecasting model (wrf). In 2010 IEEE International Geoscience and Remote Sensing Symposium, pages 2900–2903, July 2010. doi: 10.1109/IGARSS.2010.5652267.

W. Gong, F. J. Meyer, P. Webley, and D. Morton. Performance of the high-resolution atmospheric model hrrr-ak for correcting geodetic observations from spaceborne radars. Journal of Geophysical Research: Atmospheres, 118(20):11,611–11,624, 2013. doi: 10.1002/2013JD020170. URL https://agupubs.onlinelibrary.wiley.com/doi/abs/10.1002/2013JD020170.

W. Gong, F. J. Meyer, S. Liu, and R. F. Hanssen. Temporal filtering of insar data using statistical parameters from nwp models. IEEE Transactions on Geoscience and Remote Sensing, 53(7):4033–4044, July 2015. ISSN 0196-2892. doi: 10.1109/TGRS.2015.2389143.

R. F. Hanssen, T. M. Weckwerth, H. A. Zebker, and R. Klees. High-resolution water vapor mapping from interferometric radar measurements. Science, 283 (5406):1297–1299, 1999.

R.F. Hanssen. Radar Interferometry: Data Interpretation and Error Analysis. Remote Sensing and Digital Image Processing. Springer Netherlands, 2001. ISBN 9780792369455.

Eugene Hecht. Optics. Addison-Wesley, Reading, Mass, 2002. ISBN 0321188780.

HIRLAM. http://hirlam.org/index.php/hirlam-programme-53, 4 2018. URL http://www.webcitation.org/6yV6fjkzh.

Geerd-Rüdiger Hoffmann. Computer requirements for atmospheric modelling. Multiprocessing in Meteorological Models. Spinger, 1988.

Xiang-Yu Huang, Min Chen, Wei Wang, Ju-Won Kim, Bill Skamarock, and Tom Henderson. Development of digital filter initialization for wrf and its implementation at ium. 01 2007.

Isidora Jankov, William A. Gallus, Moti Segal, and Steven E. Koch. Influence of initial conditions on the wrf–arw model qpf response to physical parameterization changes. Weather and Forecasting, 22(3):501–519, 2007. doi: 10.1175/WAF998.1. URL https://doi.org/10.1175/WAF998.1.

Jungkyo Jung, Duk-jin Kim, and Sang-Eun Park. Correction of atmospheric phase screen in time series insar using wrf model for monitoring volcanic activities. Geoscience and Remote Sensing, IEEE Transactions on, 52(5): 2678–2689, May 2014. ISSN 0196-2892. doi: 10.1109/TGRS.2013.2264532.

Kakashi-Madara, 2009a. URL https://de.wikipedia.org/wiki/Datei:Elektronische_Polarisation_0.svg.

Kakashi-Madara, 2009b. URL https://de.wikipedia.org/wiki/Datei:Elektronische_Polarisation_1.svg.

Kakashi-Madara, 2009c. URL https://de.wikipedia.org/wiki/Datei:Orientierungspolarisation.svg.

Kakashi-Madara, 2009d. URL https://commons.wikimedia.org/wiki/File:Orientierungspolarisation2.svg.

Kakashi-Madara, 2009e. URL https://commons.wikimedia.org/wiki/File:Ionische_verschiebungspolarisation_0.svg.

Kakashi-Madara, 2009f. URL https://commons.wikimedia.org/wiki/File:Ionische_verschiebungspolarisation_1.svg.

J. Kouba. Improvements in Canadian Geodetic Doppler Programs. In Geodetic Symposium on Satellite Doppler Positioning, page 63, 1979.

Peter Lynch. The origins of computer weather prediction and climate modeling. Journal of Computational Physics, 227(7):3431 – 3444, 2008. ISSN 0021-9991. doi: http://dx.doi.org/10.1016/j.jcp.2007.02.034. URL http://www.sciencedirect.com/science/article/pii/S0021999107000952. Predicting weather, climate and extreme events.

Virgílio Mendes. Modeling the Neutral Atmosphere Propagation Delay in Radiometric Space Techniques. PhD thesis, 01 1999.

Ben Mills, 2006. URL https://commons.wikimedia.org/wiki/File:Water-elpot-transparent-3D-balls.png.

M. J. Moran and H. N. Shapiro. Fundamentals of engineering thermodynamics. John Wiley and Sons Inc., New York, NY, 6 edition, 2009. URL http://eu.wiley.com/WileyCDA/WileyTitle/productCd-0470540192.html.

Wolfgang E. Nagel, editor. Partielle Differentialgleichungen, Numerik und Anwendungen, volume 18, 1996. Forschungszentrum Jülich GmbH. URL http://www.fz-juelich.de/ias/jsc/EN/Expertise/Workshops/Conferences/Archive/pardiff-1996.html.

G. Nico, R. Tome, J. Catalao, and P.M.A Miranda. On the use of the wrf model to mitigate tropospheric phase delay effects in sar interferograms. Geoscience and Remote Sensing, IEEE Transactions on, 49(12):4970–4976, Dec 2011. ISSN 0196-2892. doi: 10.1109/TGRS.2011.2157511.

NOAA. https://www.ncdc.noaa.gov/data-access/model-data/model-datasets/climate-forecast-system-version2-cfsv2, 4 2018. URL http://www.webcitation.org/6yqEmnS85.

James C. Owens. Optical refractive index of air: Dependence on pressure, temperature and composition. Appl. Opt., 6(1):51–59, Jan 1967. doi: 10.1364/AO.6.000051. URL http://ao.osa.org/abstract.cfm?URI=ao-6-1-51.

D. Perissin, E. Pichelli, R. Ferretti, F. Rocca, and N. Pierdicca. The MM5 Numerical Model to Correct PSInSAR Atmospheric Phase Screen. In ESA Special Publication, volume 677 of ESA Special Publication, page 13, March 2010.

D. Perissin, F. Rocca, M. Pierdicca, E. Pichelli, D. Cimini, G. Venuti, and B. Rommen. Mitigation of atmospheric delay in insar: The esa metawave project. In 2011 IEEE International Geoscience and Remote Sensing Symposium, pages 2558–2561, July 2011. doi: 10.1109/IGARSS.2011.6049734.

N. A. Phillips. A coordinate system having some special advantages for numerical forecasting. J. Meteor., 14(2):184–185, April 1957. doi: 10.1175/1520-0469(1957)014\%3C0184:acshss\%3E2.0.co;2. URL http://dx.doi.org/10.1175/1520-0469(1957)014%3C0184:acshss%3E2.0.co;2.

E. Pichelli, R. Ferretti, D. Cimini, G. Panegrossi, D. Perissin, N. Pierdicca, F. Rocca, and B. Rommen. Insar water vapor data assimilation into mesoscale model mm5: Technique and pilot study. IEEE Journal of Selected Topics in Applied Earth Observations and Remote Sensing, 8(8):3859–3875, Aug 2015. ISSN 1939-1404. doi: 10.1109/JSTARS.2014.2357685.

N. Pierdicca, F. Rocca, P. Basili, S. Bonafoni, G. Carlesimo, D. Cimini, P. Ciotti, R. Ferretti, F. S. Marzano, V. Mattioli, M. Montopoli, R. Notarpietro, D. Perissin, E. Pichelli, B. Rommen, and G. Venuti. Synergic use of eo, nwp and ground based measurements for the mitigation of vapour artefacts in sar interferometry. In 2011 IEEE International Geoscience and Remote Sensing Symposium, pages 2566–2569, July 2011. doi: 10.1109/IGARSS.2011.6049765.

Lewis Fry Richardson. Weather prediction by numerical process. 1922.

Jean M. Rüeger. Refractive index formulae for radio waves, 2002.

Martin Silberberg. Chemistry : the molecular nature of matter and change. McGraw-Hill, Boston, 2009. ISBN 9780073048598.

William Skamarock. Evaluating mesoscale nwp models using kinetic energy spectra. Monthly Weather Review - MON WEATHER REV, 132, 12 2004. doi: 10.1175/MWR2830.1.

E.K. Smith and S. Weintraub, editors. The Constants in the Equation for Atmospheric Refractive Index at Radio Frequencies, 1953.

Gordon D. Thayer. An improved equation for the radio refractive index of air. Radio Science, 9(10):803–807, 1974. ISSN 1944-799X. doi: 10.1029/RS009i010p00803. URL http://dx.doi.org/10.1029/RS009i010p00803.

Alan Thorpe and Gerhard Adrian. Ecmwf annual report 2013. Technical report, ECMWF, 2013.

UCAR. http://www2.mmm.ucar.edu/mm5/, 4 2018a. URL http://www.webcitation.org/6yV06a5jO.

UCAR. https://www.mmm.ucar.edu/weather-research-and-forecasting-model, 4 2018b. URL http://www.webcitation.org/6yUydv4XD.

Franz-Georg Ulmer. On the accuracy gain of electromagnetic wave delay predictions derived by the digital filter initialization technique. Journal of Applied Remote Sensing, 10:10 – 10 – 7, 2016. doi: 10.1117/1.JRS.10.016007. URL https://doi.org/10.1117/1.JRS.10.016007.

Franz-Georg Ulmer and Nico Adam. A synergy method to improve ensemble weather predictions and differential sar interferograms. ISPRS Journal of Photogrammetry and Remote Sensing, 109:98 – 107, 2015. ISSN 0924-2716. doi: https://doi.org/10.1016/j.isprsjprs.2015.09.004. URL http://www.sciencedirect.com/science/article/pii/S0924271615002051.

Franz-Georg Ulmer and Nico Adam. Characterisation and improvement of the structure function estimation for application in psi. ISPRS Journal of Photogrammetry and Remote Sensing, 128:40 – 46, 2017. ISSN 0924-2716. doi: https://doi.org/10.1016/j.isprsjprs.2017.03.005. URL http://www.sciencedirect.com/science/article/pii/S0924271617302204.

Franz-Georg Ulmer and Ulrich Balss. Spin-up time research on the weather research and forecasting model for atmospheric delay mitigations of electromagnetic waves. Journal of Applied Remote Sensing, 10:10 – 10 – 12, 2016. doi: 10.1117/1.JRS.10.016027. URL https://doi.org/10.1117/1.JRS.10.016027.

Anthony David van der WAL. Evaluation of strategies for estimating residual neutral-atmosphere propagation delay in high precision global positioning system data analysis. Technical report, M.Sc.E. thesis, Department of Geodesy and Geomatics Engineering Technical Report No. 177, University of New Brunswick, Fredericton, New Brunswick, Canada., 1995.

G. Wadge, P. W. Webley, I. N. James, R. Bingley, A. Dodson, S. Waugh, T. Veneboer, G. Puglisi, M. Mattia, D. Baker, S. C. Edwards, S. J. Edwards, and P. J. Clarke. Atmospheric models, gps and insar measurements of the

tropospheric water vapour field over mount etna. Geophysical Research Letters, 29(19):11–1–11–4, 2002. doi: 10.1029/2002GL015159. URL https://agupubs.onlinelibrary.wiley.com/doi/abs/10.1029/2002GL015159.

P.W. Webley, G. Wadge, and I.N. James. Determining radio wave delay by non-hydrostatic atmospheric modelling of water vapour over mountains. Physics and chemistry of the earth, doi:10.101, 2004. URL http://centaur.reading.ac.uk/4885/.

Michael Duda Jimy Dudhia Dave Gill Michael Kavulich Kelly Keene Ming Chen Hui-Chuan Lin John Michalakes Syed Rizvi Xin Zhang Judith Berner Soyoung Ha Wei Wang, Cindy Bruyère, Janice L. Coen Kate Fossell, Jonathan D. Beezley, and Jan Mandel. User's guide for the advanced research wrf (arw) modeling system version 3.9. Technical report, UCAR, 2019.